A three-dimensional radially anisotropic model of shear velocity in the whole mantle

Mark Panning and Barbara Romanowicz

Berkeley Seismological Laboratory, University of California, Berkeley, CA 94720, USA. E-mail: mpanning@seismo.berkeley.edu

SUMMARY

We present a 3-D radially anisotropic S velocity model of the whole mantle (SAW642AN), obtained using a large three component surface and body waveform data set and an iterative inversion for structure and source parameters based on Non-linear Asymptotic Coupling Theory (NACT). The model is parametrized in level 4 spherical splines, which have a spacing of $\sim 8°$. The model shows a link between mantle flow and anisotropy in a variety of depth ranges. In the uppermost mantle, we confirm observations of regions with $V_{SH} > V_{SV}$ starting at ~80 km under oceanic regions and ~200 km under stable continental lithosphere, suggesting horizontal flow beneath the lithosphere. We also observe a $V_{SV} > V_{SH}$ signature at ~150–300 km depth beneath major ridge systems with amplitude correlated with spreading rate for fast-spreading segments. In the transition zone (400–700 km depth), regions of subducted slab material are associated with $V_{SV} > V_{SH}$, while the ridge signal decreases. While the mid-mantle has lower amplitude anisotropy (<1 per cent), we also confirm the observation of radially symmetric $V_{SH} > V_{SV}$ in the lowermost 300 km, which appears to be a robust conclusion, despite an error in our previous paper which has been corrected here. The 3-D deviations from this signature are associated with the large-scale low-velocity superplumes under the central Pacific and Africa, suggesting that $V_{SH} > V_{SV}$ is generated in the predominant horizontal flow of a mechanical boundary layer, with a change in signature related to transition to upwelling at the superplumes.

Key words: D″, radial anisotropy, tomography, transition zone, upper mantle.

1 INTRODUCTION

The 3-D seismic velocity structure of the Earth's mantle represents a snapshot of its current thermal and chemical state. As tomographic models of the isotropic seismic velocity converge in their long wavelength features (Masters *et al.* 2000; Gu *et al.* 2001; Grand 1997; Mégnin & Romanowicz 2000; Ritsema & van Heijst 2000), geodynamicists use them to infer the density structure, and thus the buoyancy contrasts which drive mantle convection (Hager 1984; Ricard & Vigny 1989; Woodward *et al.* 1993; Daradich *et al.* 2003). This process, however, is complicated by the difficulty of separating thermal and chemical contrasts, and the lack of direct sensitivity of seismic velocities to the density contrasts which drive the convection.

In many regions of the mantle, analysing the anisotropy of seismic velocities can give us another type of constraint on mantle dynamics. Nearly all the constituent minerals of the mantle have strongly anisotropic elastic properties on the microscopic scale. Random orientations of these crystals, though, tend to cancel out this anisotropy on the macroscopic scale observable by seismic waves. In general, to produce observable seismic anisotropy, deformation processes need to either align the individual crystals (lattice preferred orientation

or LPO) (e.g. Karato 1998a), or cause alignment of pockets or layers of materials with strongly contrasting elastic properties (shape preferred orientation or SPO) (Kendall & Silver 1996). While in the relatively cold regions of the lithosphere these anisotropic signatures can remain frozen-in over geologic timescales (Silver 1996), observed anisotropy at greater depths likely requires dynamic support (Vinnik *et al.* 1992). Thus, the anisotropy observed at sublithospheric depths is most likely a function of the current mantle strain field, and these observations, coupled with mineral physics observations and predictions of the relationship between strain and anisotropy of mantle materials at the appropriate pressure and temperature conditions, can help us map mantle flow.

Some of the earliest work on large-scale patterns of anisotropy focussed on the uppermost mantle. Studies showed significant *P* velocity anisotropy from body wave refraction studies (Hess 1964), as well as *S* anisotropy from incompatibility between Love and Rayleigh wave dispersion characteristics (e.g. McEvilly 1964). These observations were supported and extended globally by the inclusion of 1D radially anisotropic structure in the upper 220 km of the global reference model PREM (Dziewonski & Anderson 1981), based on normal mode observations. More recently, much upper mantle work has focussed on the observation of shear-wave splitting, particularly

in SKS phases. This approach allows for the detection and modelling of azimuthal anisotropy on fine lateral scales, but there is little depth resolution and there are trade-offs between the strength of anisotropy and the thickness of the anisotropic layer. These trade-offs make it very difficult, for example, to distinguish between models with anisotropy frozen in the lithosphere (Silver 1996) or dynamically generated in the deforming mantle at greater depths (Vinnik *et al.* 1992). Shear-wave splitting analysis has also been applied to a variety of phases to look at anisotropy to larger depths in subduction zones (Fouch & Fischer 1996). Many other studies have observed anisotropy in several geographic regions in the lowermost mantle using phases such as ScS and S_{diff} (Lay & Helmberger 1983; Vinnik *et al.* 1989; Kendall & Silver 1996; Matzel *et al.* 1997; Garnero & Lay 1997; Pulliam & Sen 1998; Lay *et al.* 1998; Russell *et al.* 1999). With observations of anisotropy in many geographical regions and at a variety of depths in the mantle, a global picture of the 3-D variation of anisotropy, such as that obtained by tomographic approaches, is desirable.

There has been increasing refinement of global 3-D tomographic models of both *P* and *S* velocity over the last 10 yr, using a variety of data sets, including absolute traveltimes, relative traveltimes measured by cross-correlation, surface wave phase velocities, free oscillations, and complete body and surface waveforms. While most of these models assume isotropic velocities, a few global anisotropic models have been developed. Upper mantle radial and azimuthal anisotropy is best resolved using fundamental mode surface waves (Tanimoto & Anderson 1985; Nataf *et al.* 1986; Montagner & Tanimoto 1991; Ekström & Dziewonski 1998; Becker *et al.* 2003; Trampert & Woodhouse 2003; Beghein & Trampert 2004) and recently with the inclusion of overtones (Gung *et al.* 2003). There are also some recent attempts at tomographically mapping transition zone radial (Beghein & Trampert 2003) and azimuthal (Trampert & van Heijst 2002) *S* anisotropy, radial S anisotropy in D″ (Panning & Romanowicz 2004) and finally *P* velocity anisotropy in the whole mantle (Boschi & Dziewonski 2000; Soldati *et al.* 2003).

In our earlier work, we have developed a complete waveform inversion technique which we used to study anisotropic structure in the upper mantle (Gung *et al.* 2003) and the core–mantle boundary region (Panning & Romanowicz 2004). Here we extend this modelling approach to map anisotropy throughout the mantle, and explore the uncertainties and implications of the model.

2 MODELLING APPROACH

2.1 Parametrization

While an isotropic elastic model requires only two independent elastic moduli (e.g. the bulk and shear moduli), a general anisotropic elastic medium is defined by 21 independent elements of the fourth-order elastic stiffness tensor. Attempting to resolve all of these elements independently throughout the mantle is not a reasonable approach, as the data are not capable of resolving so many parameters independently, and physical interpretation of such complicated structure would be far from straight-forward. For this reason, many assumptions of material symmetry can be made to reduce the number of unknowns.

A common assumption is that the material has hexagonal symmetry, which means that the elastic properties are symmetric about an axis (Babuska & Cara 1991). This type of symmetry can be used to approximate, for example, macroscopic samples of deformed olivine (the dominant mineral of the upper mantle) (Kawasaki &

Konno 1984). If the symmetry axis is arbitrarily oriented, this type of material can lead to observations of radial anisotropy (with a vertical symmetry axis), as well as azimuthal anisotropy, where velocities depend on the horizontal azimuth of propagation. However, with sufficient azimuthal coverage, the azimuthal variations will be averaged out, and we can instead focus only on the remaining terms related to a radially anisotropic model.

This reduces the number of independent elastic coefficients to 5. These have been traditionally defined by the Love coefficients: A, C, F, L and N (Love 1927). These coefficients can be related to observable seismic velocities:

$$A = \rho V_{PH}^2 \tag{1}$$

$$C = \rho V_{PV}^2 \tag{2}$$

$$L = \rho V_{SV}^2 \tag{3}$$

$$N = \rho V_{SH}^2 \tag{4}$$

$$F = \frac{\eta}{(A - 2L)}, \tag{5}$$

where ρ is density, V_{PH} and V_{PV} are the velocities of horizontally and vertically propagating *P* waves, V_{SH} and V_{SV} are the velocities of horizontally and vertically polarized *S* waves propagating horizontally, and η is a parameter related to the velocities at angles other than horizontal and vertical. Our data set of long period waveforms is primarily sensitive to V_{SH} and V_{SV}, so we use empirical scaling parameters (Montagner & Anderson 1989) to further reduce the number of unknowns to two. Because the partial derivatives with respect to the other anisotropic parameters are small, the particular choice of scaling is not critical.

Although earlier models were developed in terms of V_{SH} and V_{SV} (Gung *et al.* 2003), we choose to parametrize equivalently in terms of Voigt average isotropic *S* and *P* velocity (Babuska & Cara 1991), and three anisotropic parameters, ξ, ϕ, and η:

$$V_S^2 = \frac{2V_{SV}^2 + V_{SH}^2}{3} \tag{6}$$

$$V_P^2 = \frac{V_{PV}^2 + 4V_{PH}^2}{5} \tag{7}$$

$$\xi = \frac{V_{SH}^2}{V_{SV}^2} \tag{8}$$

$$\phi = \frac{V_{PV}^2}{V_{PH}^2} \tag{9}$$

$$\eta = \frac{F}{(A - 2L)}, \tag{10}$$

which are derived assuming small anisotropy (see Appendix A).

We invert for V_S and ξ, and scale V_P and density to V_S, and ϕ and η to ξ, using scaling factors derived from Montagner & Anderson (1989),

$$\frac{\delta \ln V_P}{\delta \ln V_S} = 0.5 \tag{11}$$

$$\frac{\delta \ln \rho}{\delta \ln V_S} = 0.33 \tag{12}$$

$$\frac{\delta \ln \eta}{\delta \ln \xi} = -2.5 \qquad (13)$$

$$\frac{\delta \ln \phi}{\delta \ln \xi} = -1.5. \qquad (14)$$

This parametrization change is made so as to invert directly for the sense and amplitude of radial anisotropy in *S* velocity, the quantity of interest. Because damping in the inversion process leads to some degree of uncertainty in the amplitudes and anisotropy is related to the difference between V_{SH} and V_{SV}, inverting for these quantities and then calculating ξ could potentially lead to considerable uncertainty in the amplitude and even the sign of the resolved anisotropy.

The model is parametrized horizontally in level 4 spherical B splines (Wang & Dahlen 1995) for both the isotropic velocity and the anisotropic parameter ξ, which is similar in spacing and number of parameters to a degree 24 spherical harmonics model. At level 4, the knots are spaced $\sim 8°$ apart. In depth, the model is parametrized in 16 cubic splines as in Mégnin & Romanowicz (2000). These splines are distributed irregularly in depth, reflecting the irregular distribution of data set sensitivity with depth, with dense coverage in the uppermost mantle due to the strong sensitivity of surface waves, and also in the core–mantle boundary region, where reflected and diffracted phases have increased sensitivity.

2.2 Theory and data set

Our approach to tomographic inversion utilizes a data set of three component long period time-domain ground acceleration seismic waveforms. These waveforms are modelled using non-linear asymptotic coupling theory (NACT) (Li & Romanowicz 1995). NACT is a normal-mode based perturbation approach, which computes coupling between modes both along and across dispersion branches. The asymptotic calculation of this coupling allows us to calculate two dimensional sensitivity kernels along the great-circle path between source and receiver. These kernels show both the ray character of phases as well as the sensitivity away from the ray-theoretical paths due to finite-frequency effects (Fig. 1).

In this study, we neglect off-plane focusing effects on the amplitudes, which we feel is reasonable since we reject data that exhibit strong amplitude anomalies, and, more importantly, our algorithm is primarily designed to fit the phase of the waveforms, which is much less affected by off-path effects than the amplitude. Capturing the 2D character of body waveform sensitivity in the vertical plane is in this case much more important than allowing for off-path effects in the horizontal plane. We also neglect the effects of azimuthal anisotropy, working from the premise that good azimuthal coverage of our data allows us to retrieve the azimuthally independent anisotropic signal. There is ample evidence for azimuthal anisotropy in the earth's mantle, and our efforts should be viewed as representing only the first step towards a complete view of global mantle anisotropy.

Expressions for the coupled mode sensitivity kernels used in this approach have been developed for models parametrized in terms of the elastic coefficients A, C, F, L and N (Li & Romanowicz 1996). The change to the radial anisotropy parametrization described above is accomplished with simple linear combinations of these kernels (Appendix A). Although for fundamental mode surface waves sensitivity is dominated by V_{SH} for transverse component data and by V_{SV} for radial and vertical components, kernels for body waves and
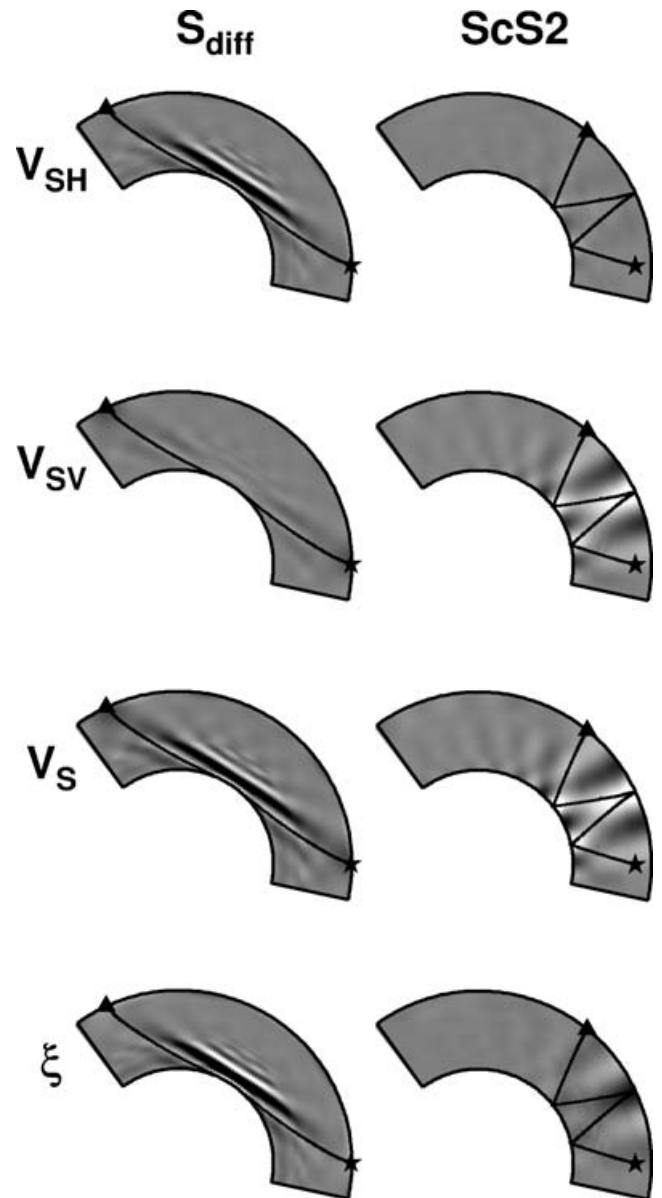

Figure 1. Kernels describing sensitivity to V_{SH} (top), V_{SV} (2nd row), isotropic V_S (third row), and ξ (bottom row) for the phases S$_{\text{diff}}$ (left) and ScS2 (right), all recorded on the transverse component. White represents positive values, black is negative, and grey is zero. The ξ kernels are multiplied by 4 to display on the same scale. The source is represented by a star, and the receiver by a triangle. The ray path from ray theory is shown as a black line. Note the dominance of V_{SH} sensitivity in the horizontally propagating S$_{\text{diff}}$, and V_{SV} in the vertical ScS2. ξ sensitivity is the same sign as V_S for S$_{\text{diff}}$, but the opposite sign for ScS2.

overtone surface waves show a much more complex sensitivity along the great-circle path (Fig. 1).

With this approach we are able to use a group velocity windowing scheme (Li & Tanimoto 1993) to efficiently synthesize acceleration wavepackets and calculate partial derivatives with respect to model parameters. Dividing the time-domain waveforms into wavepackets allows a weighting scheme that prevents larger amplitude phases from dominating the inversion. For example, separating fundamental and overtone surface wavepackets allows us to increase the weight of the overtones, increasing sensitivity in the transition zone, while increasing the weight of smaller amplitude phases, such as S$_{\text{diff}}$ and

Table 1. Summary of wavepackets used in inversion.

Wavepacket type	Component	Min. period (s)	Wavepackets	Data points
Body	Z	32	12 469	274 927
Body	L	32	9672	207 283
Body	T	32	15 076	160 627
Surface	Z	60	36 100	2, 101 379
Surface	L	60	16 373	984 183
Surface	T	60	21 101	802 913
Surface	T	80	9824	111 719
	Total		120 615	4 643 031

For component column, Z refers to vertical, L to longitudinal (along the great-circle path between source and receiver), and T to transverse (perpendicular to L). The maximum period for each wavepacket is determined by event magnitude and ranges from 220 s to 1 hr. The 80 s T surface waves represent the surface wave data set of Li & Romanowicz (1996).

multiple ScS, relative to large amplitude upper mantle phases, such as SS, increases our lowermost mantle sensitivity. The final data set consists of three-component surface and body wave packets from 1191 events (Table 1). The wavepackets were gathered using an automated picking algorithm described in Appendix B.

To assess the coverage of our data set, we calculated the sensitivity kernels for every wavepacket in our data set. For each wavepacket, we then calculated a rms average over the time-dependent sensitivity kernels and applied the weighting values used in our inversion, which account for waveform amplitude, noise and path redundancy. We then took the values for each great-circle path kernel and summed them up in a global grid with blocks 5° by 5° and approximately 200 km in depth. The geographic coverage and depth dependence of sensitivity were then plotted normalized by surface area of each cell (accounting for the smaller cells near the poles) (Figs 2a–f). In order to compare the plots of Fig. 2(a)–(f) with a ray-theoretical hit-count map, one should consider that, given our weighting system, a direct hit (i.e. a ray passing through the centre of a cell) contributes $\sim 1 \times 10^{-10}$ to 5×10^{-10} to the cells in Fig. 2

(units are s^{-1}, as the kernels represent the modal frequency shift due to a relative perturbation of a model parameter), while phases with ray theoretical paths near a cell will also contribute to the total sensitivity in that cell. The total for each depth range was also summed (Fig. 2g). Fundamental and overtone surface wave sensitivity is very strong in the upper mantle, and resolution generally decreases with depth. Note the increase in sensitivity in the lowermost 500 km due to the inclusion of phases such as S$_{diff}$ and multiple ScS. The overall sensitivity to ξ is much lower than the sensitivity to isotropic velocity, but resolution tests indicate we can resolve anisotropic structure in most depth ranges of the mantle (see Section 4.1).

Data are inverted using an iterative least-squares approach (Tarantola & Valette 1982). This approach includes *a priori* data and model covariance matrices which we can use to apply a data weighting scheme (Li & Romanowicz 1996), as well as constraints on the model norm, and radial and horizontal smoothness. Inversion iterations for anisotropic velocity structure were performed using the source parameters estimated by the Harvard CMT (Centroid Moment Tensor) project (Dziewonski & Woodhouse 1983). The reference model for our inversions is PREM (Dziewonski & Anderson 1981), with the radial Q structure of model QL6 (Durek & Ekström 1996), which has been shown to be a better fit for surface waves. Because the starting model is important in nonlinear iterative inversions, we started from the anisotropic model SAW16AN developed in Gung *et al.* (2003) to describe the upper mantle. Although this is not a whole mantle model, it was shown to provide a good fit to the surface wave and overtone data set, as well as to the body wave data set not sensitive to the core–mantle boundary region. The lower mantle of the starting model is the same as that of SAW24B16 Mégnin & Romanowicz (2000), which is a V_{SH} model derived from transverse component data. Initial convergence was achieved after three iterations, and we then selected events with a sufficient number of associated data to invert iteratively for source location, origin time and moment tensor (Li & Romanowicz 1996). Holding these parameters fixed, we recalculated the data fit for all wavepackets, adjusted the packet weighting and inverted for
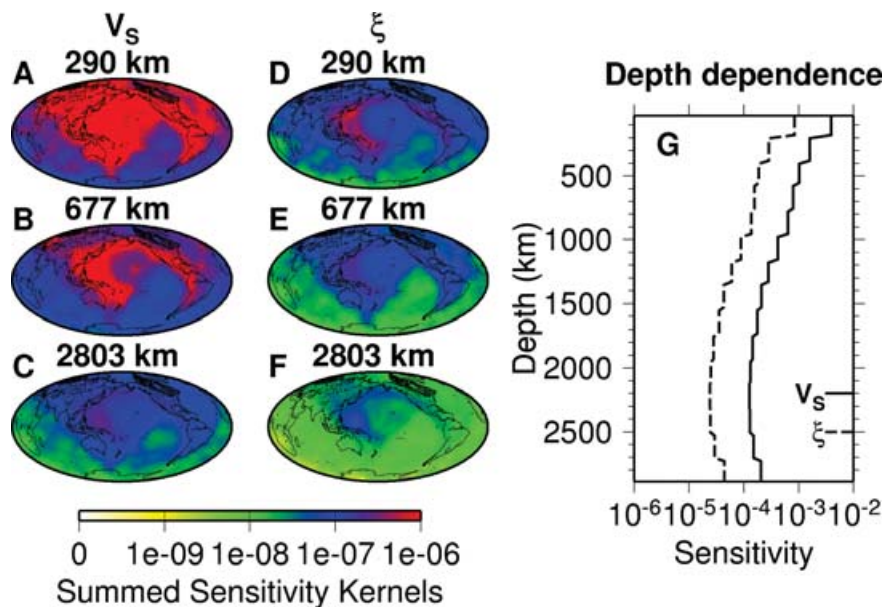

Figure 2. Coverage calculated from the summed NACT kernels of the inversion data set, as discussed in Section 2.2. The isotropic V_S and ξ coverage is shown for 200-km-thick layers in the upper mantle (A, D), lower transition zone (B, E), and lowermost mantle (C, F). The total sensitivity in each 200 km layer is shown as a function of depth (G).

structural parameters again until convergence was again reached. These initial inversions were parametrized in spherical harmonics, as in earlier work (Mégnin & Romanowicz 2000; Gung *et al.* 2003). After this, to take advantage of a new scheme for implementing non-linear crustal corrections (Marone & Romanowicz 2006), we reparametrized in spherical splines, and performed three more iterations to achieve the final model.

While the method remains much less computationally intensive than numerical approaches, the large number of wavepackets gathered (Table 1) can still require heavy computational resources. However, the calculation of the partial derivative matrix, which is the most computationally intensive step, can be very efficiently and naturally parallelized. The partial derivative matrices (multiplied by their respective transpose matrices and the *a priori* data covariance matrix) for each event can be calculated independently with minimal redundancy, and then combined linearly. Using this approach on a 32-node cluster of dual-processor machines enables us to perform model iterations in a few days, which allows us to ensure convergence as well as analyse subsets of the data to obtain estimates of the statistical error of our models.

3 MODEL RESULTS

3.1 Isotropic velocity model

The isotropic portion of the model (Fig. 3) is quite similar to previous *S* velocity tomography models. Fig. 4 shows the correlation as a function of depth with several recent tomographic models (Ekström & Dziewonski 1998; Gu *et al.* 2001; Ritsema & van Heijst 2000; Masters *et al.* 2000; Mégnin & Romanowicz 2000). The correlations in this figure were calculated by expanding each of the models in spherical harmonics up to degree 24 at the depths of the knots of the radial splines in the parametrization of SAW642AN. The correlation is then calculated over the set of spherical harmonics coefficients. The correlation is quite good with all models in the uppermost 200 km, but the models diverge somewhat in the transition zone, and more strongly in the mid-mantle range between 800 and 2000 km depth where amplitudes are low, and are closer in agreement in the lowermost mantle. The correlation is strongest with SAW24B16 (Mégnin & Romanowicz 2000), which was the starting model in the lower mantle and was derived from some common transverse component data, and SB4L18 (Masters *et al.* 2000) particularly in the lower mantle, while S362D1 (Gu *et al.* 2001) is the most divergent model, particularly in the mid-mantle. A similar pattern of correlation as a function of depth is seen when any of the other models are compared to the whole set of models, placing the isotropic portion of this model well within the scatter of previously published tomographic models. The isotropic average of S20A (Ekström & Dziewonski 1998), which is consistently in the middle of the scatter of correlation to SAW642AN, is an interesting comparison because it is an explicitly radially anisotropic model. While their inversion used isotropic sensitivity kernels, and assumed each data type was sensitive only to V_{SV} or V_{SH} structure, which is questionable for higher modes and body waves (Fig. 1), it is likely sufficient for fundamental mode surface waves, which control uppermost mantle structure. Above 400 km, the SV models of S20A and SAW642AN have an average correlation of 0.72, the SH portions are correlated at 0.71, while the cross-terms (S20A-SV to SAW642AN-SH and vice versa) are 0.67 and 0.66, meaning similar anisotropy is suggested by these two models. The isotropic average appears to have a slightly more robust agreement, though, with an average correlation of 0.75.
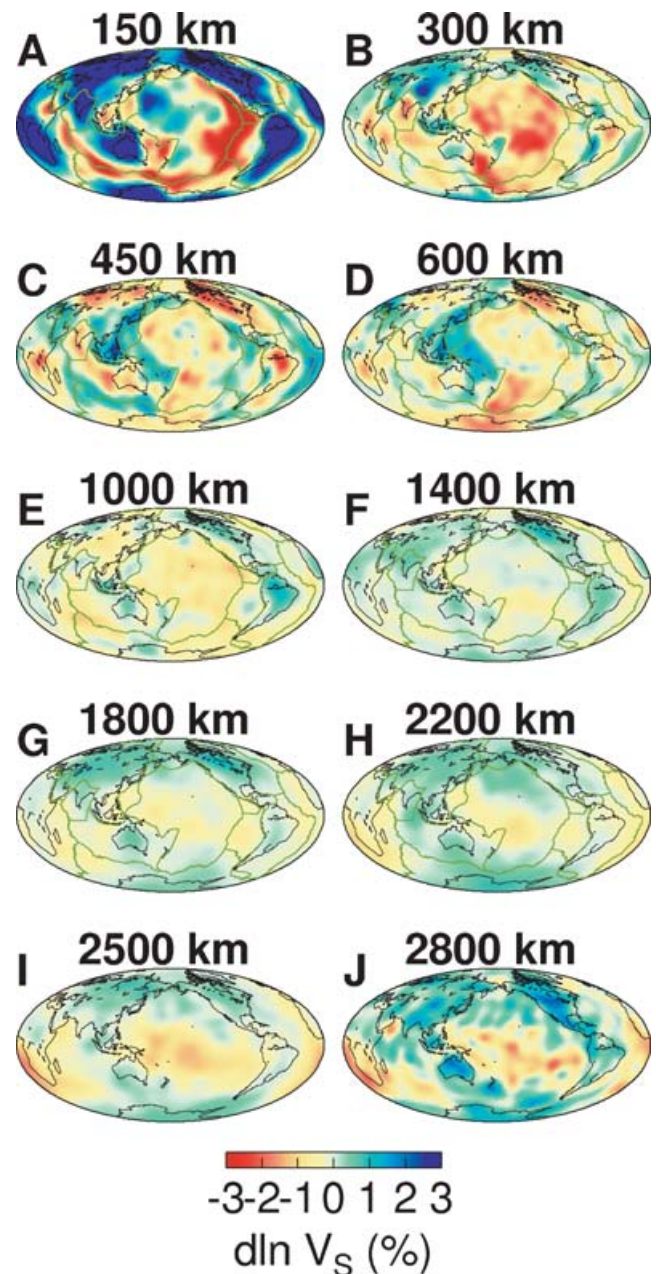
Figure 3. Isotropic V_S model at several depths.

Several common features of *S* tomographic models are present in the isotropic velocity model. The uppermost 200 km is dominated by tectonic features, with fast continents and slower oceans that show an age-dependent increase in velocity away from the slow velocities near ridges. Regions of active tectonic processes are, in general, slower, such as western North America, the major circum-Pacific subduction zones and the East African rift. In the transition zone depth range, the most prominent features are the fast velocities of subducted slabs, while the slow ridges are no longer present. Mid-mantle velocity anomalies are low in amplitude, and more white in spectrum. Finally, in the lowermost 500 km, the amplitudes of heterogeneity increase again, and become dominated by a degree 2 pattern with rings of higher velocities surrounding two lower velocity regions under the central Pacific and Africa, commonly referred to as superplumes.
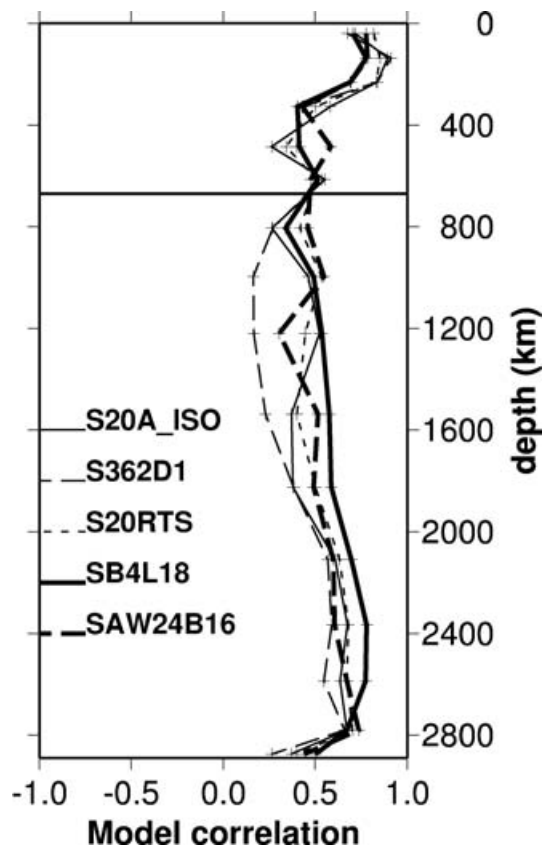
Figure 4. Correlation of isotropic velocity model with previously published V_S tomographic models.

To a first-order approximation, data fit only depends on the isotropic component of the model; accordingly, tomographic results for V_S are quite stable, and maintain their character whether or not anisotropy is included in the model. The isotropic portion of SAW642AN leads to a variance reduction in the waveforms of 48.4 per cent, while adding anisotropy improves the variance reduction to 52.1 per cent (Table 2). While this improvement in fit is significant above the 99 per cent confidence level according to an F-test criterion (Menke 1989) (given the large number of degrees of freedom of our modelling), the isotropic model is obviously the most important control. As a demonstration of the stability of the isotropic structure, we inverted for isotropic models without anisotropy at several points in our iterative approach, and the resulting models were consistently correlated with the isotropic portion of the anisotropic

model from the same iteration above 0.9 at all depth ranges in the mantle.

Given this first-order sensitivity to the isotropic structure and the lower sensitivity to ξ of the data set (Fig. 2), it is reasonable to question the stability of the inversion for ξ structure. To test this, we held the damping fixed for V_S and varied the damping for ξ an order of magnitude in either direction. As expected this caused large changes in amplitude of ξ structure recovered (average rms amplitude smaller by a factor of 4 for the increased damping, and larger by $\sim$10 per cent for the reduced damping), but the patterns were quite stable with an average correlation to the SAW642AN structure of 0.86 for the overdamped case, and above 0.99 for the underdamped case. When the ξ damping was fixed, and the V_S damping was changed, the ξ structure was even more stable, with negligible changes in amplitude and correlations above 0.999 when V_S was underdamped and 0.95 when V_S was significantly overdamped. The correlation did drop to 0.88 over the transition zone when V_S was overdamped, suggesting that this is a depth range where we need to be aware of potential trade-offs.

3.2 Upper mantle anisotropy

The ξ structure above 300 km (Figs 5a–c) is similar to that of Gung *et al.* (2003) (hereafter referred to as GPR03), with an average correlation coefficient of 0.53 across this depth range. However, there are some differences in the structures when they are compared in detail (Fig. 5). The amplitudes are lower by roughly 50 per cent at shallow depths (note the saturation in Figs 5d–f). This is primarily due to the fact that in the current model, the ξ parameter is damped directly rather than being derived from the difference of SV and SH velocity models. Damping was chosen such that the overall amplitude of damping coefficients was similar for both V_S and ξ, leading to lower ξ amplitudes than in the previous model. The positive $\delta \ln \xi$ signature under oceans observed previously (Montagner & Tanimoto 1991; Ekström & Dziewonski 1998) is constrained to slightly shallower depths, while the continental root signature is more pronounced at 300 km depth. This adds greater support to the idea of $V_{SH} > V_{SV}$ anisotropy generated in the asthenosphere at different depths beneath the oceanic and continental lithosphere advanced in GPR03. The addition of body wave data not included in the modelling of GPR03 apparently sharpens these asthenospheric features, but to obtain this sharpness it was important to include non-linear crustal corrections (see Marone & Romanowicz 2006, and Section 4.3). Earlier iterations that included only linear crustal corrections showed a much more vertically smeared structure in the upper mantle.

Table 2. Percent variance reduction for data subsets.

Data set	SAW642AN	Model A	Model B	Model C	SAW24B16
Fundamental modes	60.8	60.1	60.0	55.2	23.7
Overtones	48.7	48.4	48.2	47.4	40.8
Total surface waves	56.2	55.7	55.5	52.2	30.2
Body waves	44.8	43.7	43.0	41.4	22.2
CMB sensitive	48.2	46.9	46.6	45.8	29.5
Total	52.1	51.4	51.1	48.4	27.4

Models A through C are models where the anisotropic structure is progressively stripped from the fully anisotropic model. Model A removes all anisotropic structure below 1000 km, Model B has no anisotropic structure below 300 km, and Model C has no anisotropic structure beyond the reference model. CMB sensitive data refers to the body wave packets that sample the CMB region, such as Sdiff, ScS, and SKS. SAW24B16 is the SH velocity model of Mégnin & Romanowicz (2000).
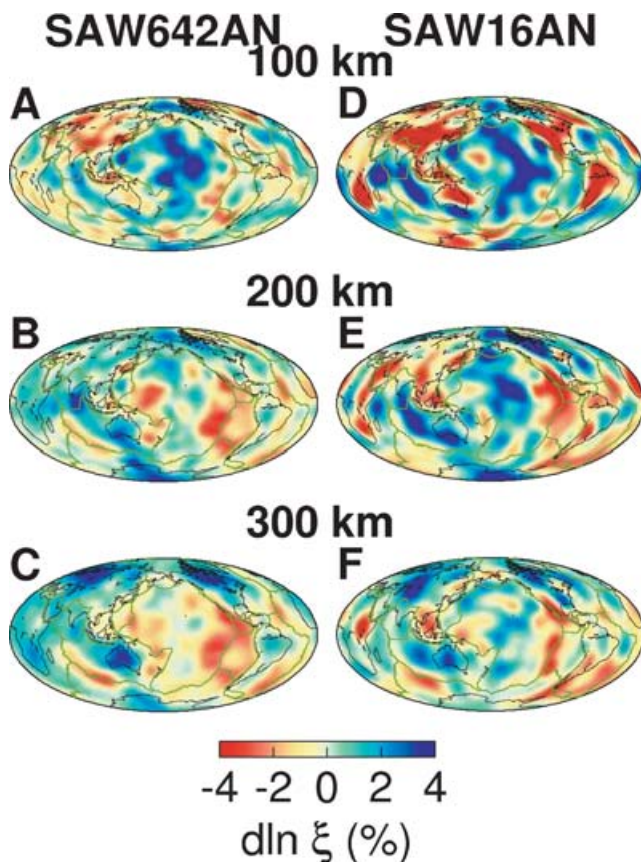
Figure 5. Comparison between SAW642AN ξ from this paper (A–C) and the upper mantle ξ calculated from SAW16AN (Gung *et al.* 2003) (D–F) at depths of 100 (top), 200 (middle), and 300 km (bottom).

In the new model, a negative $\delta \ln \xi$ signature is associated with the ridges between 150 and 300 km depth. For the fast-spreading ridges of the Pacific and Indian Oceans in particular, there appears to be a strong correlation between the amplitude of the negative $\delta \ln \xi$ signature and the spreading rate of the ridge. To quantify this relationship, we defined a series of ridge segments approximately 750 km in length for all major mid-ocean ridges. For each segment we compared the value of $\delta \ln \xi$ with the spreading rate. Spreading rates were calculated by taking the component of relative velocity perpendicular to each ridge segment as calculated using NUVEL-1 (DeMets *et al.* 1990) evaluated at the midpoint of each segment. For quantitative comparison purposes, we used all segments with spreading rates greater than 5 cm yr^{-1} (displayed in bold solid and dashed lines in Fig. 6), all of which are located in the Pacific and Indian Oceans. The spreading rates compared with $\delta \ln \xi$ values at 150 and 200 km depth are shown in Fig. 7. Most values are negative, although there are a few positive values corresponding to segments along the ridge between Australia and Antarctica, which we will discuss later. If we perform a linear regression on the correlation of the $\delta \ln \xi$ values at 150 and 200 km depth compared with the spreading rates, we fit the data with R^2 values (a measure of goodness-of-fit which ranges from 0 to 1, with 1 meaning a perfect fit) of 0.25 and 0.24, respectively. Given the number of segments used in the regression, both of these values represent a significant relationship between $\delta \ln \xi$ and spreading rate just above the 99 per cent confidence level according to an F-test. The p-values, which indicate the probability that the misfit of the linear regression is equivalent to a line with a slope of zero, are 0.008 and 0.007 for
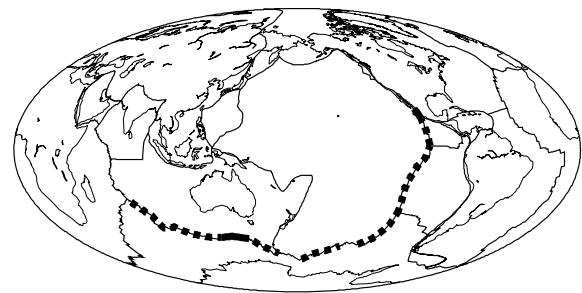

Figure 6. Fast-spreading ridge segments used in spreading rate calculations. Segments in bold solid and dashed lines represent all segments with spreading rates faster than 5 cm yr^{-1} used in Fig. 7. The solid segments on the northern EPR and near the Australia-Antarctic discordance are also shown in Fig. 7, but are excluded in some regression calculations.
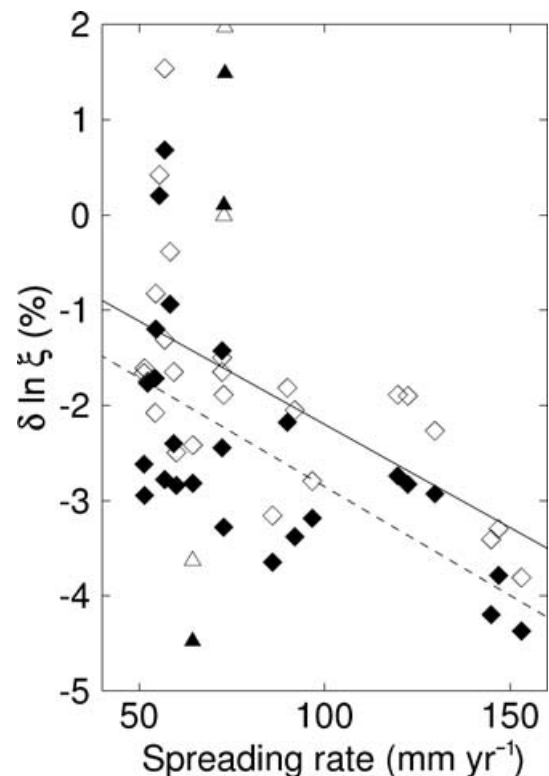

Figure 7. Spreading rate vs. model $\delta \ln \xi$ value for the segments shown in Fig. 6. Segments used for linear regression are shown with diamonds, while the three segments not used in the regression (solid segments in Fig. 6) are triangles. Model $\delta \ln \xi$ values are shown at 150 km (open symbols) and 200 km (filled symbols), and the regression lines are shown for the data at 150 km (solid) and 200 km (dashed).

150 and 200 km respectively. However, there are three segments that appear reasonable to exclude from the fit (solid lines in Fig. 6 and triangles in Fig. 7). The northernmost segment of the East Pacific rise represents a segment that is intersecting a subduction zone, and has an anomalously low value of $\delta \ln \xi$, perhaps due to complications related to the subduction zone. Additionally, there are two segments corresponding to the complex Australian–Antarctic Discordance (AAD) (Christie *et al.* 1998) that have anomalously high $\delta \ln \xi$. Interestingly, this area is topographically depressed compared to other ridge segments, which would be consistent with less-than-expected feeding flow to the ridge segment. Note that the segments along this plate boundary to the east of the AAD also appear to

have anomalously high $\delta \ln \xi$ values, but they were not excluded from the regression, as they are well beyond the anomalous topography associated with the AAD, and there was therefore no obvious geological reason to exclude them from the fit. When these three segments are excluded from the regression analysis, the R^2 values increase to 0.40 for both 150 and 200 km depth. This represents a significant relationship above the 99.9 per cent confidence level, with p-values equal to 0.0008. This significant correlation between the variation of surface spreading rates along several ridge systems and amplitude of anisotropy at depth strongly supports development of $V_{SV} > V_{SH}$ due to vertical flow beneath fast-spreading mid-ocean ridges. In some slower spreading regions, we still observe $V_{SH} > V_{SV}$, characteristic of the horizontal deformation usually seen away from the ridges under oceanic regions.

3.3 Transition zone anisotropy

While anisotropy in the transition zone (400–700 km) is not included in global models such as PREM (Dziewonski & Anderson 1981), several studies have indicated the possible presence of anisotropy in this depth range (Montagner & Kennett 1996; Fouch & Fischer 1996; Trampert & van Heijst 2002; Beghein & Trampert 2003). While the amplitudes observed in our model are lower than those in the uppermost mantle (Fig. 8), there is an anisotropic signature present in this depth range.

A prominent feature of the model in this depth range (Fig. 9) is the association of negative ξ perturbation ($V_{SV} > V_{SH}$) with subduction zones. Below 400 km depth, there is a broad association of negative ξ perturbations with many of the high isotropic velocities which correspond well with the predicted locations of slabs from a geodynamic model based on reconstructed subduction history over the last 180 Myr (Lithgow-Bertelloni & Richards 1998) (Fig. 9). This signature fades rapidly below the 670 discontinuity,
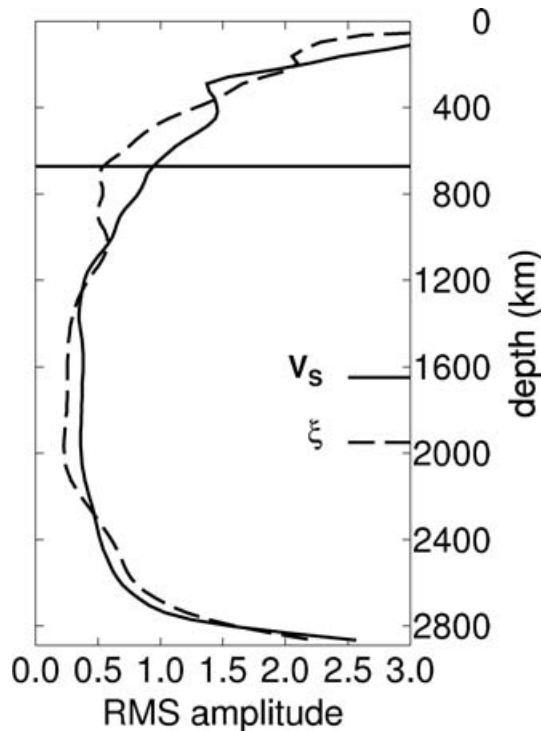

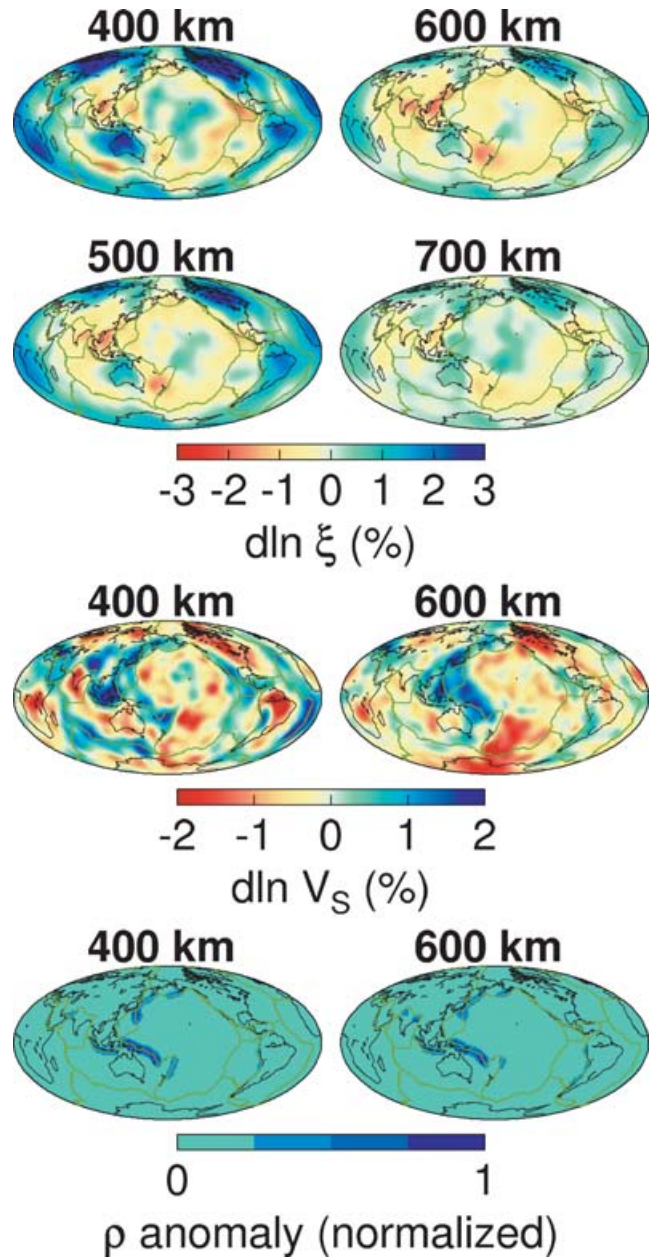**Figure 9.** ξ structure at depths 400–700 km (top two rows) and V_S structure at depths of 400 and 600 km (third row). The bottom row shows the density anomalies for 145 km thick layers centred at depths of 362.5 km (left) and 652.5 km (right) for the model of Lithgow-Bertelloni & Richards (1998), normalized to the maximum density anomaly in each depth range.

even though some isotropic velocity anomalies continue. These observations suggest that quasi-vertical flow in the subduction zones may lead to observed anisotropy, perhaps through a mechanism related to alignment of spinel crystals or through alignment of pockets of strongly contrasting garnetetite derived from oceanic crust (Karato 1998b). It is important to note, however, that this signal appears to vary greatly between subduction zones. For example, the isotropic signal in South America is less pronounced than western Pacific subduction zones. The negative ξ signal is not apparent at all under South America, while it is much more obvious in the Central American and western Pacific subduction zones.

The ridge signal of negative ξ anomalies, which is prominent

Figure 8. The rms amplitudes as a function of depth in SAW642AN for V_S (solid) and ξ (dashed).

in the uppermost 300 km of the model, decreases in amplitude with depth, although it does not disappear until depths greater than 500 km. The isotropic anomaly, however, does not extend to such depths. The slow decay of the ξ signature, when combined with evidence from isotropic velocity (Montagner & Ritsema 2001) and attenuation models (Romanowicz & Gung 2002) that ridge-feeding features are constrained to be shallow, suggests that there may be large vertical smearing in this depth range, although it is not obvious in resolution tests (Section 4.1).

Fouch & Fischer (1996) also observed anisotropy in the transition zone depth range from shear wave splitting measurements of local *S* and teleseismic SKS associated with some (but not all) subduction zones in the Northwest Pacific. Specifically, there was evidence for splitting extending to at least 480 km and perhaps through the transition zone into the uppermost lower mantle under the Southern Kuril arc (Sakhalin Island), as well as possibly beneath western Honshu in Japan, although the anisotropy was constrained to shallower depths beneath the Izu-Bonin trench to the south, where our model does show some negative ξ perturbation. As these were splitting measurements, they only measured azimuthal anisotropy in a horizontal plane, so the sense of anisotropy cannot be directly compared.

There are some differences when comparing our model to other global models of transition zone anisotropy. The radially symmetric pattern of our model (Fig. 10) differs from that of Montagner & Kennett (1996), who inverted for 1D anisotropic structure. They observed a signal of positive ξ perturbations above the 670 changing to negative perturbations below the 670, while our model shows a signal small in amplitude but opposite in sign. While the earlier work on low-degree azimuthal anisotropy in the transition zone by Trampert & van Heijst (2002) is not directly comparable, we note that general amplitude levels of $\sim$2 per cent are compatible with both studies. Beghein & Trampert (2003) also look at radial anisotropy in the transition zone, although they do not present a single preferred
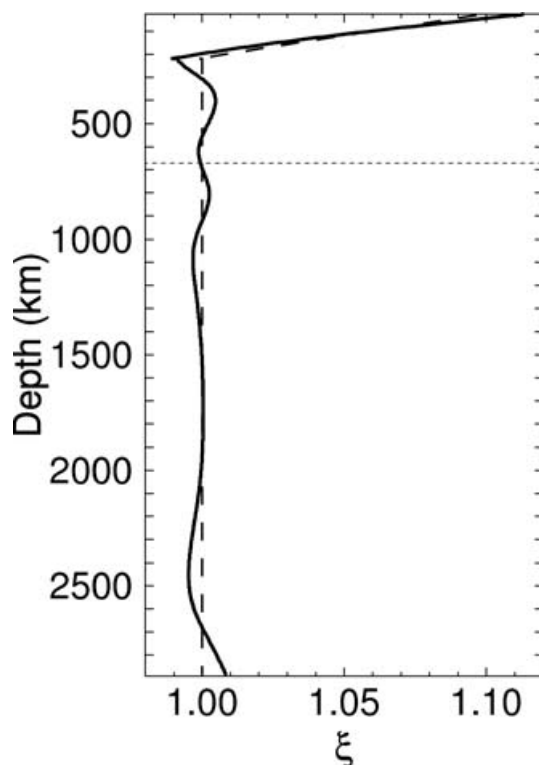
structural model. They choose to look at the distribution of likely models grouped over large tectonically defined regions, making a direct comparison difficult. While this approach does not obviously show the subduction-related anisotropic signature, their modelling only includes fundamental and overtone surface waves. The addition of body waves in our data set greatly improves the sampling, particularly in subduction regions.

3.4 Lower mantle anisotropy

The amplitude of anisotropic structure in the model in the bulk of the lower mantle is lower than that of both the lowermost mantle and the upper mantle. Mineral physics and seismology studies suggest that the bulk of the lower mantle is nearly isotropic (Meade *et al.* 1995). While anisotropic structure is included throughout the lower mantle in our model for completeness, amplitudes are low between 1000 and 2500 km depth (Fig. 8), and resolution is questionable (Section 4.1). In earlier modelling efforts (Panning 2004), we showed that when inverting for models with this region constrained to be isotropic, the change in fit to the data was small with no effect on surface waves and less than 0.3 per cent change to the fit of the body waveforms. Little change was seen in the anisotropic structure of other depth ranges. Anisotropic structure in this depth range is likely not well resolved in our modelling, and it does not appear to be required by the data.

The final model in the lowermost mantle (Fig. 11) is similar in low degrees to the model of anisotropic structure for the core–mantle boundary (CMB) region developed in Panning & Romanowicz (2004), hereafter referred to as PR04, which was constrained to structure spherical harmonics degree 8 for lower-mantle ξ. As in that model, the radially symmetric term is prominent (Fig. 10), and corresponds to a positive ξ anomaly ($V_{SH} > V_{SV}$) on the order of 1 per cent throughout the depth range. The large-scale pattern is also fairly similar (correlation coefficient of 0.51 for expansion up to degree 8 averaged over the bottom 300 km). There are many differences in relative amplitude, and while some of these, such as the differences beneath Antarctica and southern Africa, occur in areas of poor coverage (Fig. 2), there are also noticeable differences in the central Pacific and central Asia where the coverage is much better.

Although the model parametrization is the same in PR04, and the data set is similar, the inversions leading to the two models differ primarily in two respects. The PR04 model was a single iteration model using Harvard CMT solutions, while multiple iterations were performed for the model discussed in this paper, as well as inversion for source parameters for most events. Even more importantly, the scaling of V_P and ρ to V_S and η and ϕ to ξ in the PR04 model was not correctly applied in the inversion code, with V_P and ρ scaling coefficients mistakenly interchanged with η and ϕ coefficients. Despite the considerable difference in scaling used, including a change of sign, the results are similar, and the radially symmetric structure is robust. It does appear, however, that this may be an important consideration in certain geographic regions where there are strong differences between the PR04 model and the current model, and this conclusion is supported by an earlier test we performed where we inverted for lower resolution models where ϕ and η structure was either inverted for independently or fixed to that of the anisotropic *P* model of Soldati *et al.* (2003) (Panning 2004), where the greatest variations seem to be in the same geographic regions. This suggests that great care be exercised when interpreting the detailed 3-D anisotropic structure in the CMB region, as there are few constraints
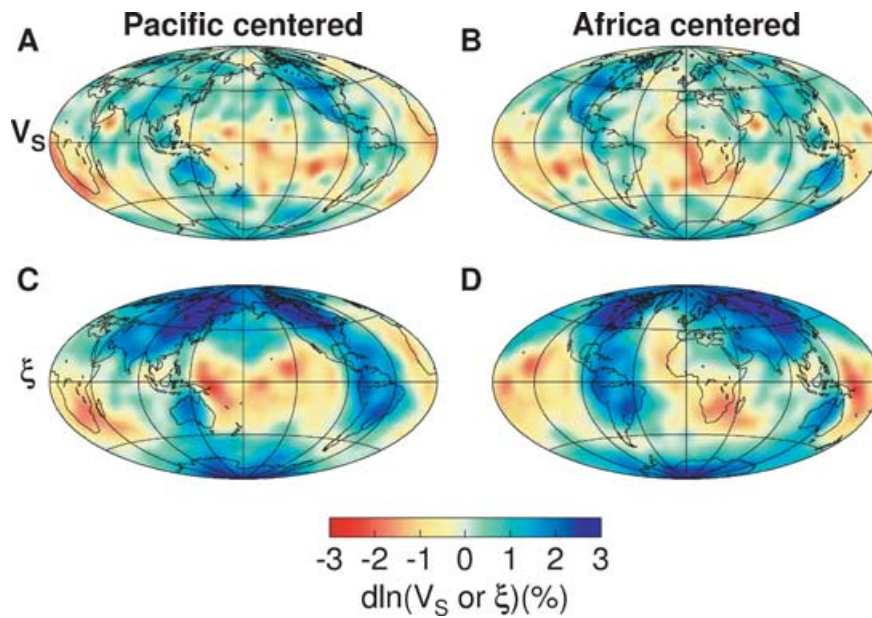

Figure 10. Average ξ signature as a function of depth.

Figure 11. V_S (A, B) and ξ structure (C, D) at a depth of 2800 km centred under the central Pacific (A, C) and Africa (B, D).

on what scaling coefficients to use, and it is difficult to constrain the ϕ and η structure independently given our data set.

Previous studies have also shown that CMB topography can exhibit trade-offs with anisotropic structure (Boschi & Dziewonski 2000). This does not appear to be a strong concern for our data set, however. During the development of our earlier models (Panning 2004), we inverted for topography on both the CMB and the 670 discontinuity simultaneously with velocity structure, and the recovered model was strongly correlated with the model without discontinuity topography at correlations above 0.99 in the CMB region, with only minor perturbations to relative amplitudes.

In PR04, it was noted that the two broad regions that most deviated from the average signature corresponded to the superplume regions of low isotropic velocity, although there were also regions of reduced ξ west of North America and under central Asia. In this improved model, the deviations seem to be even more closely associated with the superplumes, while the central Asia anomaly has disappeared, and the anomaly west of North America has become less pronounced.

Although these observations do not uniquely constrain the mineral physics or dynamics of the lowermost mantle, they remain suggestive of a model where considerable anisotropy is generated in the primarily horizontal flow at the mechanical boundary layer under downgoing slabs, either through a mechanism of LPO (McNamara *et al.* 2002; Iitaka *et al.* 2004; Tsuchiya *et al.* 2004) or SPO (Kendall & Silver 1996). Recent theoretical and experimental studies have also demonstrated the possible stability of post-perovskite phase of $MgSiO_3$ in the lowermost 300 km of the mantle (Iitaka *et al.* 2004; Tsuchiya *et al.* 2004). This phase may have a greater single crystal elastic anisotropy at lowermost mantle pressures than the perovskite thought to make up the bulk of the lower mantle, at least for 0 Kelvin theoretical work (Iitaka *et al.* 2004), although work with analogue materials suggest it is questionable whether post-perovskite will slip in a mechanism favourable to the production of large anisotropy (Merkel *et al.* 2006).

Regardless of the mechanism responsible for the horizontal flow signature under the slabs, as the material approaches regions of large-scale upwelling this signature changes, and we see a reduction

in observed anisotropy, with negative $\delta \ln \xi$ regions observed under the superplumes. There are a number of possible mechanisms for this, including rotation of the anisotropic material (McNamara *et al.* 2002), inclusions of vertically oriented melt pockets, or different anisotropic behaviour of potentially chemically distinct material at the base of the superplumes.

4 MODEL RESOLUTION AND ERROR

4.1 Resolution matrix tests

A common way of analysing the resolution of a model from a least-squares inversion is to utilize the resolution matrix. Using this approach, it is possible to get an idea of the model resolution given the data set's sensitivity, and the *a priori* damping scheme applied. It does not, however, assess uncertainties resulting from the theoretical approximations in the partial derivative calculation, or due to errors in the data aside from the effect of the *a priori* data covariance matrix applied as a weighting factor to the data points in the inversion.

Given these limitations, this approach allows us to perform the standard 'checkerboard' tests to obtain an estimate of the geographical resolution of the model parameters. The isotropic velocity model effectively recovers anomalies at spacings of less than 1500 km in the upper mantle, but the resolution is not as good in the mid-mantle, particularly in the southern hemisphere where coverage is poorer. We examine the output model for an input checkerboard with spacings that vary as a function of depth between 1200 and 3000 km (Fig. 12a) at a variety of depths both with (Fig. 12c) and without (Fig. 12b) anisotropy in the input model. The pattern is well captured, although there is some reduction in amplitude. The resolution for ξ is, not surprisingly, not as good (Fig. 13). The shortest wavelength structure is not resolved at all, except in the shallowest depth ranges. For the mid-mantle, the input checkerboard model only includes anomalies at ~5000 and ~7000 km, and even this structure is strongly reduced in amplitude and potentially sensitive to trade-offs with isotropic velocity structure (Fig. 13c). However, the resolution
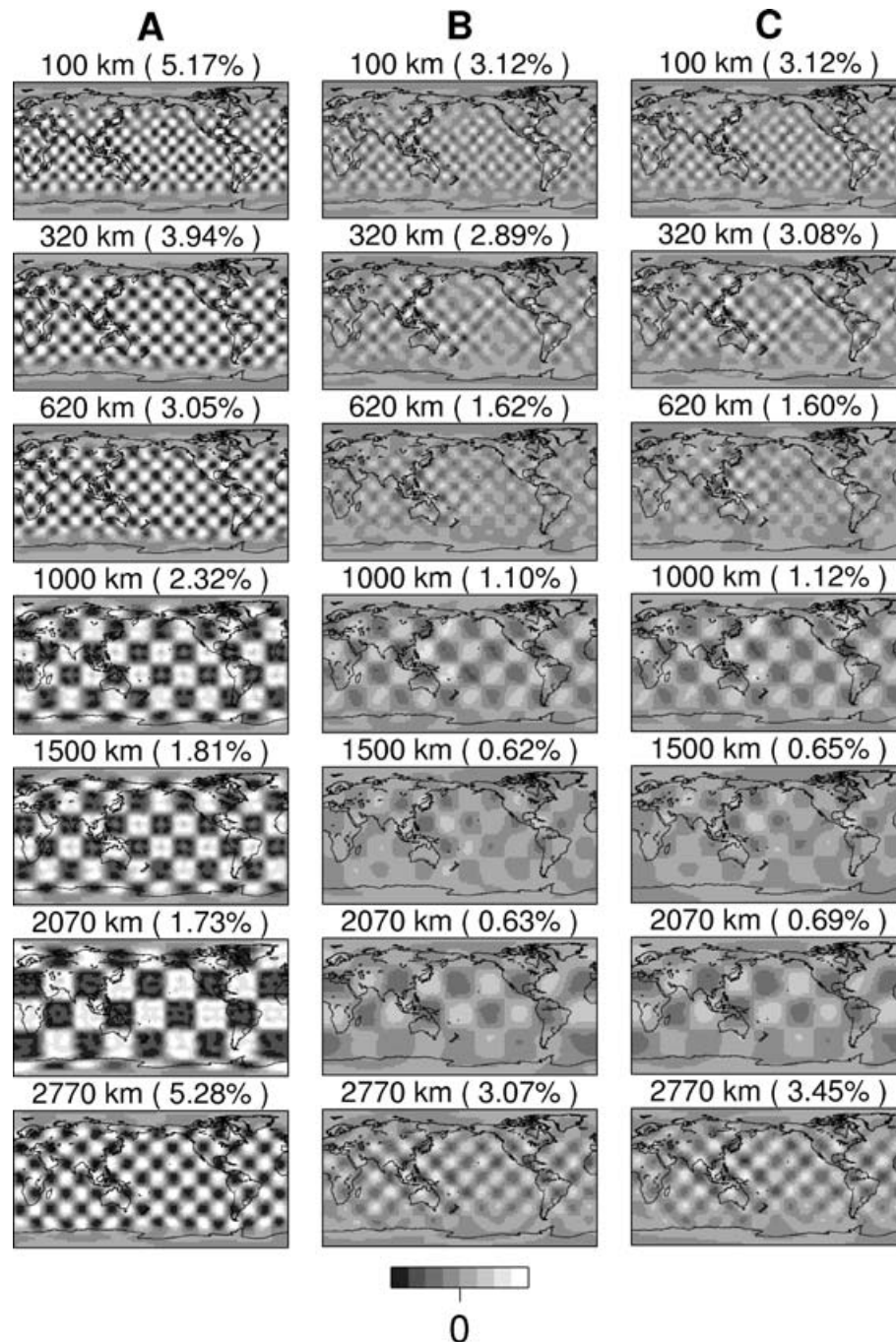
Figure 12. Resolution matrix checkerboard test for isotropic V_S structure. The input model (column A) produces the output structure in column B, when no anisotropic structure is included in the input, and the model in column C when anisotropic structure is also present in the input model. Numbers in parentheses are the maximum amplitude for each map. The shading is scaled to the maximum amplitude in column A for each depth.

improves in the lowermost mantle with good recovery of structure with wavelengths down to 2500 km.

We also tested the depth resolution of the modelling. We used an input model of random ξ structure assigned to each spline coefficient and compared the input and output amplitude as a function of depth (Fig. 14). For each depth range, there is some amount of smearing, although a more noticeable effect is the loss of amplitude, particularly in the lower mantle. This is due to the relatively conservative damping scheme that was chosen to ensure stability of the inversion since ξ sensitivity is consistently smaller than isotropic V_S

sensitivity (Fig. 2). Structure in either of the two splines corresponding to the deepest mantle (Figs 14g, h) maps into a similar pattern with a peak at the CMB. This confirms that the depth distribution of the anisotropy found in the lowermost mantle is poorly resolved, as already discussed in PR04.

4.2 Bootstrap and jackknife error estimates

Formal errors are difficult to calculate for model parameters in a damped least-squares inversion. One way to estimate the model
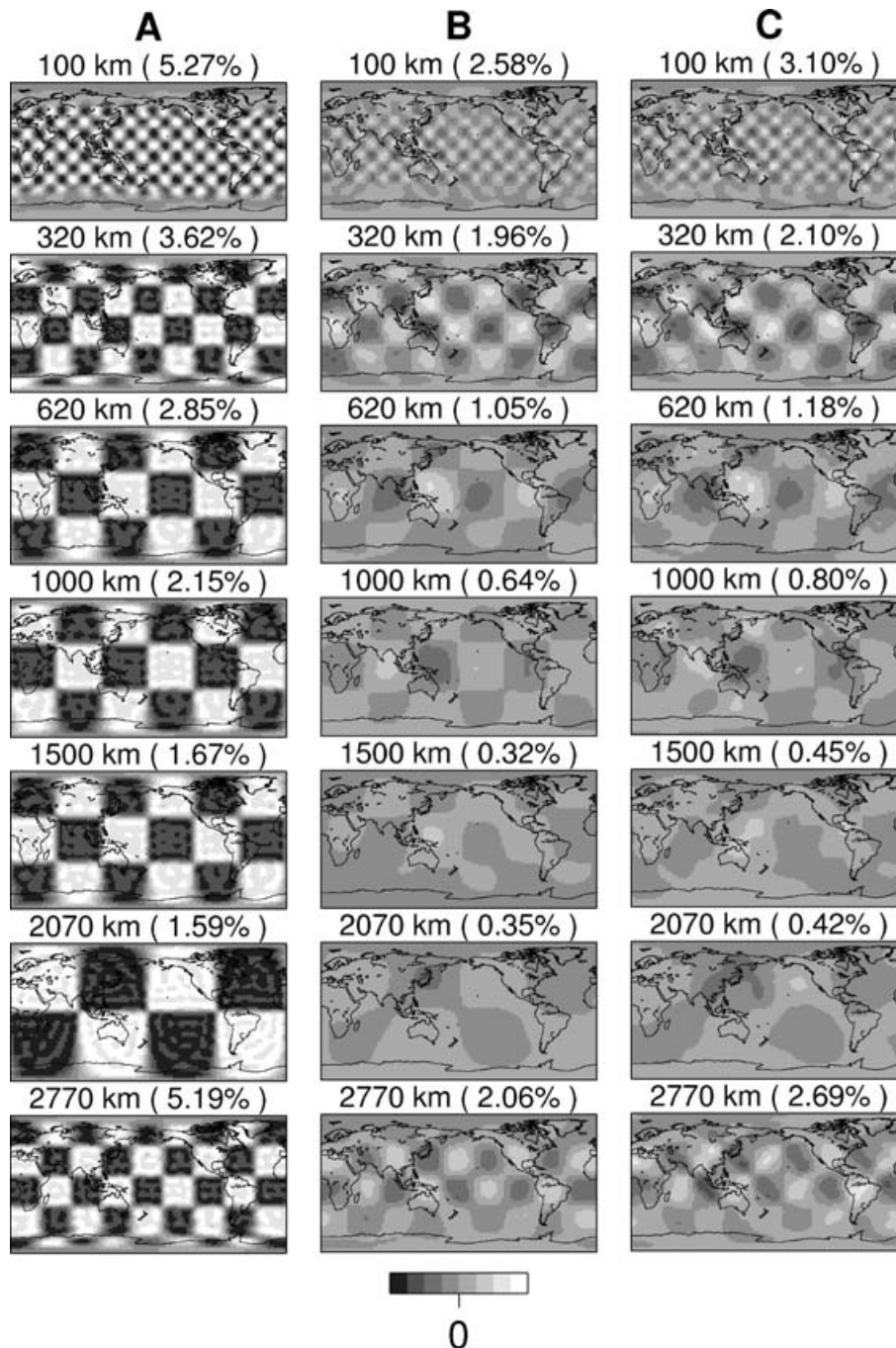
Figure 13. Same as Fig. 12 for ξ structure. The input model (column A) does not include isotropic structure for the output in column B, but does for column C.

errors, given our inversion process is through a bootstrap approach (Efron & Tibishirani 1993). The bootstrap is a general statistical approach to calculating the standard error of the value of any estimator, θ. In our case, θ is the set of partial derivative and matrix calculations leading from the data set of seismic waveforms to our model. The bootstrap standard error is calculated by applying the estimator to a sufficiently large set of random samples of the data, and computing the standard deviation of the models estimated from each sample. Although our data set has millions of points (Table 1), we simplify this approach by considering 12 subsets of the data formed by separating the data by the month of the event, and considering those as our sample population. A bootstrap sample is then any set

of 12 subsets selected from that population with replacement. For any set of n observations, there are n^n bootstrap samples, although many of these are exchangeable (i.e. $x_1, x_2, \ldots x_n$ is the same as $x_2, x_1, \ldots x_n$). Even taking into account that exchangeability, there are more than 1 300 000 possible bootstrap samples of our 12 subsets, which is far too many to reasonably calculate, but the bootstrap approach will in general converge relatively quickly. We choose to make 312 bootstrap resamples, and then generate maps of the estimated errors (Fig. 15).

A similar approach which is somewhat less computationally intensive is the deleted jackknife error estimation. In this approach, the model is calculated for a series of n data sets which leave out d
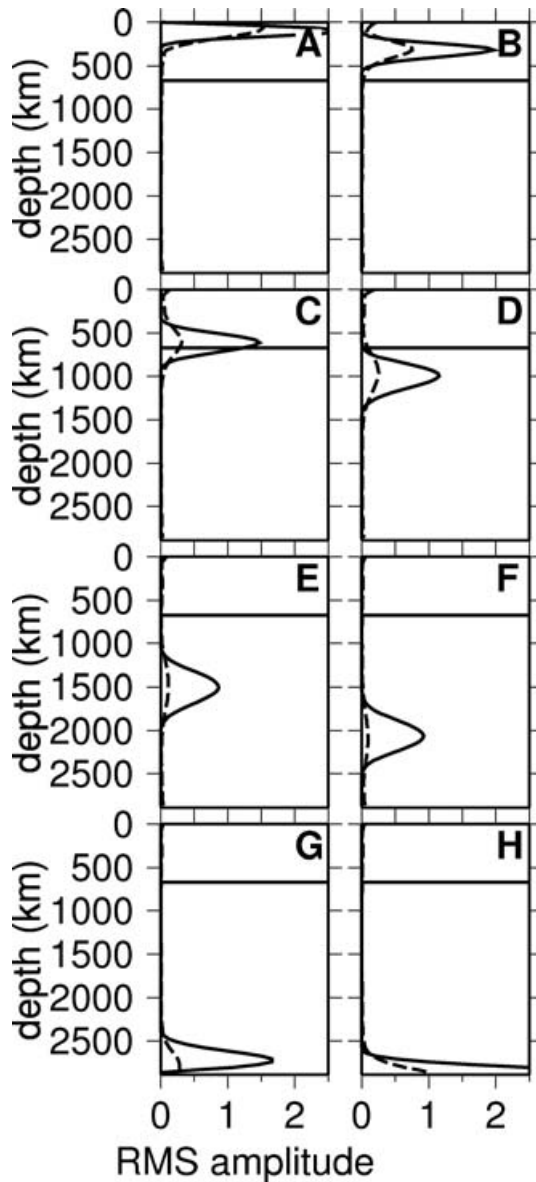
Figure 14. Resolution matrix test where input ξ structure is constrained to a single radial spline. Input amplitude (solid line) and output (dashed line) is shown for splines with peak amplitudes at 121 (A), 321 (B), 621 (C), 996 (D), 1521 (E), 2096 (F) and 2771 km depth (G), as well as at the CMB (H).

observations at a time, and the standard error is calculated as

$$\hat{se}_{\text{jack}} = \sqrt{\frac{n-d}{d \cdot C(n,d)} \sum (\theta_{(i)} - \bar{\theta})},$$

where $C(n, d)$ is combinatorial notation indicating the number of subsets of size d from a population of n chosen without replacement, the sum is over the $C(n, d)$ possible jackknife samples of the data set, $\theta_{(i)}$ is the estimator value for the ith jackknife sample, and $\bar{\theta} = \sum \theta_{(i)}/(C(n, d))$. This is basically the standard deviation of the models multiplied by an inflation factor roughly equal to n for $d = 1$ and smaller values for $d > 1$, where the data sets are less similar to the original data set. If we use the same 12 subsets as above, only 12 models need to be calculated for $d = 1$, or 66 for $d = 2$.

All three estimates of the error in the maps are virtually identical, with a correlation above 0.99 at all depth ranges, and amplitudes

within a few percent. Therefore we only show the error maps from the bootstrap approach. The consistency of the three estimates is a crosscheck that we performed enough bootstrap resamples. The error estimate for isotropic V_S is consistently low throughout the mantle, with a small increase in the lowermost mantle (compare error amplitude in Fig. 15k with model amplitude in Fig. 8). In general, there does not appear to be a strong geographic bias in the V_S error maps, although there is a slightly larger error in the lowermost mantle in the southern hemisphere where the coverage is poorest. The ξ errors are larger in the upper mantle, but similar to the errors in V_S in the lower mantle. The pattern is different, though, with the largest error in the upper mantle associated with gradients of structure within the Indian and Pacific Ocean basins. In the lowermost mantle, the largest errors are in general correlated with the regions of highest amplitude; however, it is interesting to note that one of the regions with the most significant error is the central Pacific where we notice a large difference between SAW642AN and the model from PR04, further suggesting that this is a complicated region that the data may not resolve well on this scale.

Our approach to error estimation does not directly treat errors related to the changes in the choice of damping or theoretical assumptions. Instead, these error maps give an estimate of how random errors in the data map into the observed structure, given the damping and inversion scheme used to develop the model. There is an inherent trade-off between the resolution and error of the model, as relaxing the *a priori* damping will allow greater theoretical resolution both in terms of amplitude and wavelength of structure, but will also increase the sensitivity of the model to errors in the data, leading to a larger standard error estimate.

4.3 Other sources of error

4.3.1 Crustal corrections

An important consideration in any study of mantle structure is that of corrections for crustal structure. Surface waves are strongly sensitive to crustal structure, and previous studies have shown that even the sensitivity of long-period surface waves at depths as large as 200 km can be affected by the local crustal structure (Boschi & Ekström 2002). Approximating the effect of the crust as a linear perturbation from a single reference model is inadequate. For this reason, we have chosen to implement a non-linear crustal correction scheme in this modelling (Montagner & Jobert 1988; Marone & Romanowicz 2006). In this approach, we first regionalize the crustal models based on CRUST 2.0 (Bassin *et al.* 2000) (Fig. 16). We defined the regions based on criteria evaluating crustal thickness and average V_P, V_S and density, and then created average models for each region. The solid crust was divided into three layers, with the top one corresponding to the sediment layers and upper crust of CRUST 2.0, and the bottom two corresponding to the middle and lower crust of CRUST 2.0. Average thicknesses and velocities of each of these three layers as well as the ocean layer are computed from CRUST 2.0 to define the model for each larger region (Fig. 17). Frequency shifts computed in NACT, which are used to define the partial derivatives, are defined by integrals of a local frequency shift along the great-circle path between source and receiver. This local frequency shift is now defined as a non-linear shift plus a linear shift. The non-linear shift is based on the difference between the mode frequency in the appropriate regional crustal model and PREM. The linear shift includes further linear corrections for deviations of the Moho and seafloor from the regional model plus contributions from
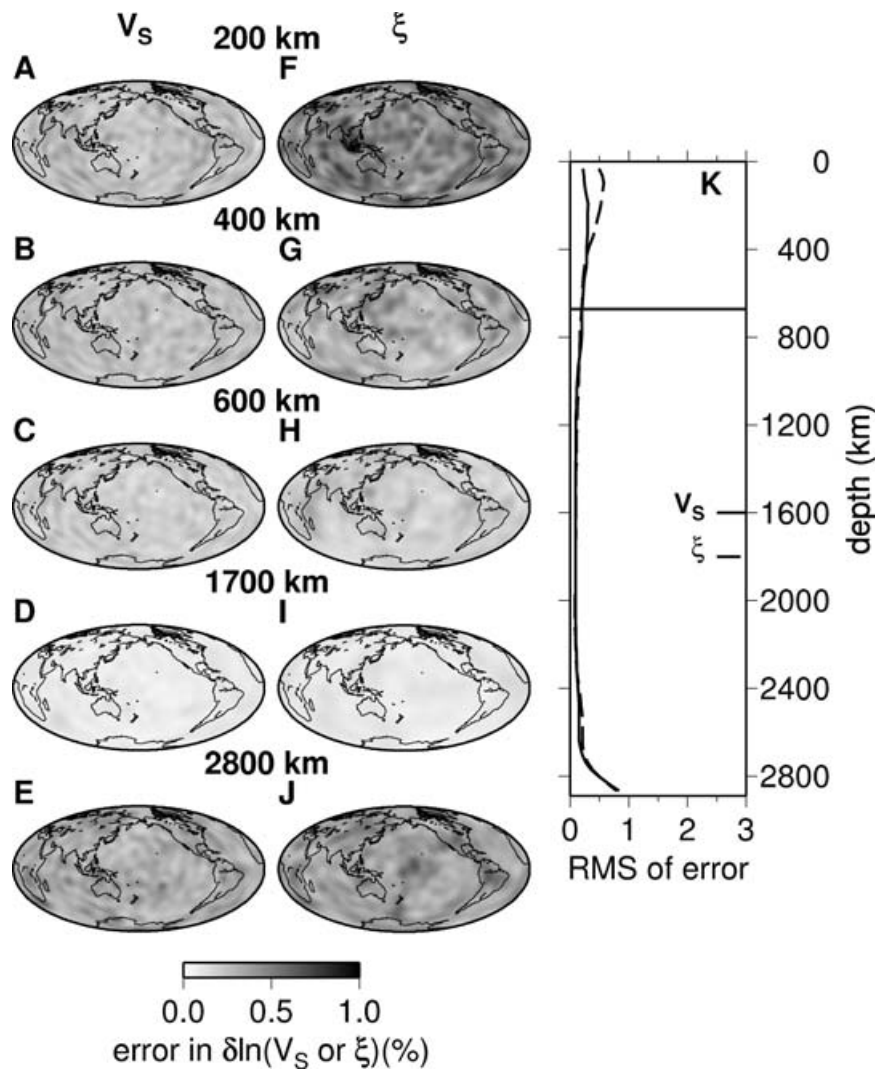
Figure 15. Standard error of model values calculated using a bootstrap algorithm at several depths for V_S (A–E) and ξ (F–J). The RMS amplitude of the standard error as a function of depth (K) is also shown for V_S (solid) and ξ (dashed), and can be compared with amplitudes of the model structure shown in Fig. 8. Note that the errors are quoted in percent perturbation from the reference model, not as percentages of the final model amplitudes. The colour scale is not saturated.

3-D structure at depth computed using sensitivity kernels appropriate for the local crustal structure. This means that for each point along the path, the sensitivity kernels will vary based on the overlying crustal structure. While this study does not undertake a systematic exploration of the impact of this crustal correction, previous work has shown that it appears to sharpen images in the upper mantle, particularly in anisotropic structure (Marone & Romanowicz 2006).

4.3.2 Scaling parameters

The anisotropic scaling parameters used in our modelling were derived for deformation of upper mantle materials above 400 km (Montagner & Anderson 1989). Obviously, it is reasonable to question the validity of this scaling assumption at greater depths. We tested the influence of the assumed scaling parameters in earlier modelling work, before applying the current non-linear crustal corrections. We performed tests with the ϕ model fixed to that of Soldati *et al.* (2003). We then scaled the 3-D η structure to this ϕ model.

For our first test, we fixed the ϕ and η structures, and then inverted the pre-source inversion data set for low-degree ξ structure starting from a model with no ξ perturbations. We also performed an inversion where the ξ, ϕ, and η structures were simultaneously inverted starting from the ξ model used in the source inversions, and the ϕ and η model described above.

In general, the ξ models derived in these tests agreed well with the equivalent ξ model derived using the same source parameters and crustal corrections, especially in the lower mantle. The strongest deviations occurred for the fixed ϕ and η model in the region immediately above and below the 670 discontinuity, where correlation dropped below 0.5. This suggests that this region could exhibit strong trade-offs with ϕ and η structure, as well as potentially unmodelled azimuthal anisotropy. It is also possible that this instability could be related to a distinct change in structure characteristics on either side of the 670 discontinuity (e.g. Gu *et al.* 2001) which is unmodelled in our smooth radial spline parametrization. In any case, interpretation of anisotropy in the lower transition zone and uppermost lower mantle should be undertaken with a degree of caution.
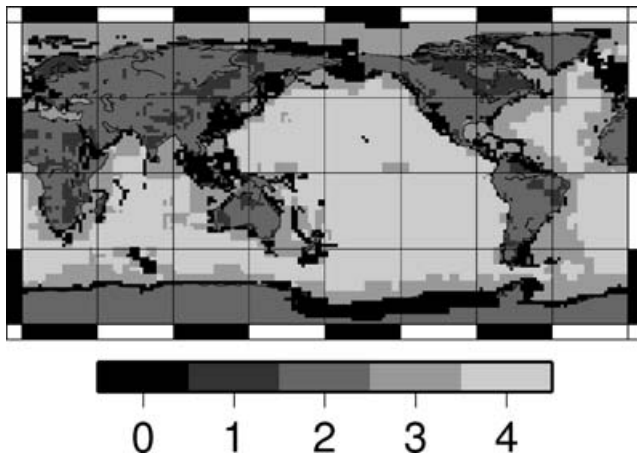
Figure 16. Crustal regionalization scheme used for non-linear crustal corrections. The crust model was separated into different types in 2° by 2° blocks using CRUST 2.0.
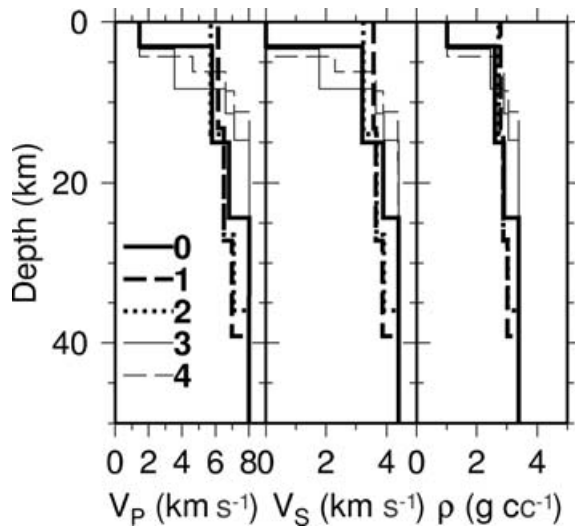

Figure 17. The average crustal models used in the non-linear crustal correction. The model numbers correspond to the regionalization displayed in Fig. 16.

4.3.3 Model parametrization

For our final model, we chose to parametrize shear velocity anisotropy in terms of the Voigt average isotropic velocity and ξ. Some previous models of anisotropy, particularly in the upper mantle have preferred a parametrization with separate V_{SV} and V_{SH} models (Ekström & Dziewonski 1998; Gung *et al.* 2003). This is a natural parametrization choice for models with a large fundamental mode surface wave data set, as the parametrization directly mirrors the sensitivity of the data set. However, with a data set also containing overtone surface waves and body waves to model whole mantle structure, the division of data set sensitivity is no longer so obvious, and damping considerations favour a model where we invert directly for the anisotropy, so as to not map errors in amplitude of velocity structure into an anisotropic signature.

To examine this effect, we inverted for V_{SV} and V_{SH} separately, starting from V_{SV} and V_{SH} models converted from an earlier it-

eration V_S and ξ model. The isotropic average of the resulting V_{SV}/V_{SH} model was very consistent with high correlations above 0.9. The anisotropic structure was also stable in the upper mantle, but exhibited some differences in the transition zone (correlation dropped to 0.89), and was much less well correlated in the mid-mantle depth range with correlation values near 0.5. There was also a pronounced increase in the amplitude and radial roughness of recovered anisotropy in the lower mantle, because we were not directly damping ξ. This large amplitude signature in the mid-mantle depth ranges is hard to reconcile with studies showing negligible anisotropy in the bulk of the lower mantle. The lowermost mantle anisotropy derived from the V_{SV}/V_{SH} model had a similar average profile as the preferred model, but the amplitudes of 3-D heterogeneity were more variable, and the correlation averaged 0.8.

5 ANALYSIS OF VARIANCE

The variance reduction estimates of SAW642AN are presented for the various subsets of our data (Table 2). For comparison, we also show the variance reduction for the model SAW24B16 (Mégnin & Romanowicz 2000), which was developed using similar theory but with only transverse component data and was the starting model for the lower mantle. Note that the variance reduction for SAW24B16 using this data set is much less than that quoted in the original paper. The chief differences in the data set are the fact that we use three-component data, use non-linear crustal corrections and use source mechanisms that were updated to fit the three-component data set in an anisotropic model, as well as including more events and surface waveforms to higher frequency. If we restrict ourselves to T component data, SAW24B16 variance reduction increases to 36.4 per cent, and if we use linear crustal corrections and the crustal model used in the original modelling, the variance reduction improves to 48.6 per cent, which is comparable to that obtained for the original data set.

To get an idea of how important the anisotropy in various depth ranges is for the different subsets of the data, we also present variance reduction estimates for models with the anisotropic structure progressively stripped out. It is clear that the uppermost mantle anisotropic structure is the most important for improving the fit to the data, but other depth ranges also improve the fit for various subsets of the data. It is difficult, however, to reliably determine whether a given model has a statistically significant improvement in fit over a model with a different number of parameters. In principle, we can use an F test (Menke 1989), but in order to do so, we must decide on how many degrees of freedom there are in the two models compared. We can simply subtract the number of model parameters from the number of data points, which would suggest that our modelling has millions of degrees of freedom, meaning that all of the anisotropic structure is significant above the 99 per cent confidence level. However, this does not take into account that not all of the data points are independent, and that damping effectively reduces the number of model parameters. Additionally, for a fair comparison, we should reinvert our data for a best fitting model with anisotropy constrained to zero in various depth ranges rather than just stripping the anisotropy from a best-fitting anisotropic model. Such an attempt was made in our earlier modelling (supplementary material to PR04) based on similar variance estimates, which suggested, for example, that the CMB anisotropy did produce a statistically significant improvement in fit to the CMB sensitive component of the body wave data set.

6 CONCLUSIONS

The isotropic velocities of SAW642AN are compatible with previous tomographic models of shear velocity structure and are quite stable regardless of the anisotropic structure. The anisotropic portion of the model can be related to mantle flow patterns in several depth ranges throughout the mantle.

Specifically, a positive $\delta \ln \xi$ signature appears consistent with a region of likely horizontal flow under the lithosphere at different depths for oceans and old continents (Gung *et al.* 2003). A negative $\delta \ln \xi$ signature at 150–300 km depth is associated with spreading ridge segments, and the amplitude is significantly correlated with surface spreading rates for fast-spreading segments. There is also negative $\delta \ln \xi$ correlated with subducting slabs in the transition zone, although this depth range appears to be sensitive to trade-offs with unmodelled anisotropic velocity parameters, as well as potentially with isotropic structure if V_S is overdamped. Mid-mantle anisotropy is lower in amplitude, and its inclusion does not significantly affect the patterns obtained in other depth ranges. The structure near the CMB is dominated by a radially symmetric positive $\delta \ln \xi$, likely due to horizontal flow in a mechanical boundary layer, with deviations associated with the low-velocity superplumes.

Although the current data set cannot provide us with anisotropic resolution at the same level as global isotropic velocity models, and some trade-offs with parameters not modelled here remain, the additional information can help constrain geodynamic models, and provide an opportunity to verify and guide the experimental and theoretical findings of mineral physics.

ACKNOWLEDGMENTS

REFERENCES

Babuska, V. & Cara, M., 1991. *Seismic Anisotropy in the Earth*, Kluwer Academic Press, Boston, Massachusetts.

Bassin, C., Laske, G. & Masters, G., 2000. The current limits of resolution for surface wave tomography in North America, *EOS, Trans. AGU,* **81,** F897.

Becker, T.W., Kellogg, J.B., Ekström, G. & O'Connell, R.J., 2003. Comparison of azimuthal seismic anisotropy from surface waves and finite strain from global mantle-circulation models, *Geophys. J. Int.,* **155,** 696–714.

Beghein, C. & Trampert, J., 2003. Probability density functions for radial anisotropy: implications for the upper 1200 km of the mantle, *Earth Planet. Sci. Lett.,* **217,** 151–162.

Beghein, C. & Trampert, J., 2004. Probability density functions for radial anisotropy from fundamental mode surface wave data and the neighbourhood Algorithm, *Geophys. J. Int.,* **157,** 1163–1174.

Boschi, L. & Dziewonski, A., 2000. Whole Earth tomography from delay times of P, PcP, PKP phases: lateral heterogeneities in the outer core, or radial anisotropy in the mantle?, *J. Geophys. Res.,* **104,** 25267–25594.

Boschi, L. & Ekström, G., 2002. New images of the Earth's upper mantle from measurements of surface wave phase velocity anomalies, *J. Geophys. Res.,* **107,** 2059, doi:10.1029/2002GL016647.

Christie, D.M., West, B.P., Pyle, D.G. & Hanan, B.B., 1998. Chaotic to-

pography, mantle flow and mantle migration in the Australian-Antarctic discordance, *Nature,* **394,** 637–644.

Daradich, A., Mitrovica, J.X., Pysklywec, R.N. Willett, S.D. & Forte, A.M., 2003. Mantle flow, dynamic topography, and rift-flank uplift of Arabia, *Geology,* **30,** 901–904.

DeMets, C., Gordon, R.G., Argus, D.F. & Stein, S., 1990. Current plate motions, *Geophys. J. Int.,* **101,** 425–478.

Durek, J.J. & Ekström, G., 1996. A radial model of anelasticity consistent with long-period surface-wave attenuation, *Bull. seism. Soc. Am.,* **86,** 144–158.

Dziewonski, A.M. & Anderson, D.L., 1981. Preliminary Reference Earth Model, *Phys. Earth Planet. Inter.,* **25,** 297–356.

Dziewonski, A.M. & Woodhouse, J.H., 1983. Studies of the seismic source using normal-mode theory, in *Earthquakes: observation, theory and interpretation*, pp. 45–137, eds Kanamori, H. & Boschi, E., North-Holland Publ. Co., Amsterdam, The Netherlands.

Efron, B. & Tibishirani, R.J., 1991. *An Introduction to Bootstrap*, Chapman and Hall, New York.

Ekström, G. & Dziewonski, A.M., 1998. The unique anisotropy of the Pacific upper mantle, *Nature,* **394,** 168–172.

Fouch, M.J. & Fischer, K.M., 1996. Mantle anisotropy beneath northwest Pacific subduction zones, *J. Geophys. Res.,* **101,** 15987–16002.

Garnero, E.J. & Lay, T., 1997. Lateral variations in lowermost mantle shear wave anisotropy beneath the north Pacific and Alaska, *J. geophys. Res.,* **102,** 8121–8135.

Grand, S., 1997. Global seismic tomography: a snapshot of convection in the Earth, *GSA Today,* **7,** 1–7.

Gu, Y.J., Dziewonski, A.M., Su, W. & Ekström, G., 2001. Models of the mantle shear velocity and discontinuities in the pattern of lateral heterogeneities, *J. Geophys. Res.,* **106,** 11169–11199.

Gung, Y., 2003. *Lateral variations in attenuation and anisotropy of the upper mantle from seismic waveform tomography*, PhD thesis, University of California at Berkeley, Berkeley, California.

Gung, Y., Panning, M. & Romanowicz, B., 2003. Global anisotropy and the thickness of continents, *Nature,* **422,** 707–711.

Hess, H., 1964. Seismic anisotropy of the uppermost mantle under oceans, *Nature,* **203,** 629–631.

Hager, B.H., 1984. Subducted slabs and the geoid – constraints on mantle rheology and flow, *J. geophys. Res.,* **89,** 6003–6015.

Iitaka, T., Hirose, K., Kawamura, K. & Murakami, M., 2004. The elasticity of the $MgSiO_3$ post-perovskite phase in the Earth's lowermost mantle, *Nature,* **430,** 442–445.

Karato, S.-I., 1998a. Some remarks on the origin of seismic anisotropy in the D'' layer, *Earth Planets Space,* **50,** 1019–1028.

Karato, S.-I., 1998b. Seismic anisotropy in the deep mantle, boundary layers and the geometry of mantle convection, *Pure Appl. Geophys.,* **151,** 565–587.

Kawasaki, I. & Konno, F., 1984. Azimuthal anisotropy of surface waves and the possible type of seismic anisotropy due to preferred orientation of olivine in the uppermost mantle beneath the Pacific ocean, *J. Phys. Earth,* **32,** 229–244.

Kendall, J.-M. & Silver, P.G., 1996. Constraints from seismic anisotropy on the nature of the lowermost mantle, *Nature,* **381,** 409–412.

Lay, T. & Helmberger, D.V., 1983. The shear-wave velocity gradient at the base of the mantle, *J. geophys. Res.,* **88,** 8160–8170.

Lay, T., Williams, Q., Garnero, E.J., Kellogg, L. & Wysession, M.E., 1998. Seismic wave anisotropy in the D" region and its implications, in *The Core-Mantle Boundary Region*, pp. 299–318, eds Gurnis, M., Wysession, M.E., Knittle, E. & Buffett, B.A., Amer. Geophys. Union, Washington, DC.

Li, X.D. & Romanowicz, B., 1995. Comparison of global waveform inversions with and without considering cross-branch modal coupling, *Geophys. J. Int.,* **121,** 695–709.

Li, X.D. & Romanowicz, B., 1996. Global mantle shear velocity model developed using nonlinear asymptotic coupling theory, *J. Geophys. Res.,* **101,** 22245–22272.

Li, X.D. & Tanimoto, T., 1993. Waveforms of long-period body waves in a slightly aspherical Earth model, *Geophys. J. Int.,* **112,** 92–102.

Lithgow-Bertelloni, C. & Richards, M.A., 1998. The dynamics of Cenozoic and Mesozoic plate motions, *Rev. Geophys.,* **36,** 27–78.

Love, A.E.H., 1927. *A Treatise on the Theory of Elasticity*, Cambridge Univ. Press, Cambridge.

Marone, F. & Romanowicz, B.A., 2006. Non-linear crustal corrections in high resolution regional waveform seismic tomography, *Geophys. J. Int.*, in revision.

Masters, G., Laske, G., Bolton, H. & Dziewonski, A., 2000. The relative behavior of shear velocity, bulk sound speed, and compressional velocity in the mantle: implications for chemical and thermal structure, in *Earth's Deep Interior*, AGU Monograph 117, pp. 63–86, eds. Karato, S., Forte, A.M., Liebermann, R.C., Masters, G. & Stixrude, L., Amer. Geophys. Union, Washington, DC.

Matzel, E., Sen, K. & Grand, S.P., 1997. Evidence for anisotropy in the deep mantle beneath Alaska, *Geophys. Res. Lett.,* **23,** 2417–2420.

McEvilly, T.V., 1964. Central U.S. crust-upper mantle structure from Love and Rayleigh wave phase velocity inversion, *Bull. Seism. Soc. Amer.,* **54,** 1997–2015.

McNamara, A.K., van Keken, P.E. & Karato, S.-I., 2002. Development of anisotropic structure in the Earth's lower mantle by solid-state convection, *Nature,* **416,** 310–314.

Meade, C., Silver, P.G. & Kaneshima, S., 1995. Laboratory and seismological observations of lower mantle isotropy, *Geophys. Res. Lett.,* **22,** 1293–1296.

Mégnin, C. & Romanowicz, B.A., 2000. The 3D shear velocity structure of the mantle from the inversion of body, surface and higher mode waveforms, *Geophys. J. Int.,* **143,** 709–728.

Menke, W.H., 1989. *Geophysical Data Analysis: Discrete Inverse Theory, Revised Ed.*, Academic Press, Inc., New York.

Merkel, S., Kubo, A., Miyagi, L., Speziale, S., Duffy, T.S., Mao, H. & Wenk, H.-R., 2006. Plastic deformation of MgGeO$_3$ post-perovskite at lower mantle pressures, *Science,* **311,** 644–646.

Mochizuki, E., 1986. The free oscillations of an anisotropic and heterogeneous Earth, *Geophys. J. R. astr. Soc.,* **86,** 167–176.

Montagner, J.-P. & Jobert, N., 1988. Vectorial tomography; II. Application to the Indian Ocean, *Geophys. J. R. astr. Soc.,* **94,** 295–307.

Montagner, J.-P. & Anderson, D.L., 1989. Petrological constraints on seismic anisotropy, *Phys. Earth Planet. Inter.,* **54,** 82–105.

Montagner, J.-P. & Kennett, B.L.N., 1996. How to reconcile body-wave and normal-mode reference earth models, *Geophys. J. Int.,* **125,** 229–248.

Montagner, J.-P. & Ritsema, J., 2001. Interactions between ridges and plumes, *Science,* **294,** 1472–1473.

Montagner, J.-P. & Tanimoto, T., 1991. Global upper mantle tomography of seismic velocities and anisotropies, *J. Geophys. Res.,* **96,** 20337–20351.

Nataf, H.-C., Nakanishi, I. & Anderson, D.L., 1986. Measurements of mantle wave velocities and inversion for lateral heterogeneities and anisotropy: 3. inversion, *J. Geophys. Res.,* **91,** 7261–7307.

Panning, M.P., 2004. *Deep Earth seismic structure and earthquake source processes from long period waveform modeling*, Ph.D. thesis, University of California at Berkeley, Berkeley, California.

Panning, M.P. & Romanowicz, B.A., 2004. Inferences on flow at the base of Earth's mantle based on seismic anisotropy, *Science,* **303,** 351–353.

Pulliam, J., Sen, M.K., 1998. Seismic anisotropy in the core-mantle transition zone, *Geophys. J. Int.,* **135,** 113–128.

Revenaugh, J. & Jordan, T.H., 1987. Observations of first-order mantle reverberations, *Bull. seism. Soc. Am.,* **77,** 1704–1717.

Ricard, Y. & Vigny, C., 1989. Mantle dynamics with induced plate tectonics, *J. Geophys. Res.,* **94,** 17543–17560.

Ritsema, J. & van Heijst, H.-J., 2000. Seismic imaging of structural heterogeneity in Earth's mantle: evidence for large-scale mantle flow, *Science Progress,* **83,** 243–259.

Romanowicz, B. & Gung, Y., 2002. Superplumes from the core-mantle boundary to the lithosphere; implications for heat flux, *Science,* **296,** 513–516.

Romanowicz, B. & Snieder, R., 1988. A new formalism for the effect of lateral heterogeneity on normal modes and surface waves-II. General anisotropic perturbation, *Geophys. J. Int.,* **93,** 91–99.

Russell, S.A., Lay, T. & Garnero, E.J., 1999. Small-scale lateral shear velocity and anisotropy heterogeneity near the core-mantle boundary beneath the central Pacific imaged using broadband ScS waves, *J. geophys. Res.,* **104,** 13183–13199.

Silver, P.G., 1996. Seismic anisotropy beneath the continents: probing the depths of geology, *Annu. Rev. Earth Planet. Sci.,* **24,** 385–432.

Soldati, G., Boschi, L. & Piersanti, A., 2003. Outer core density heterogeneity and the discrepancy between PKP and PcP travel time observations, *Geophys. Res. Lett.,* **30**, 10.1029/2002GL016647..

Tanimoto, T. & Anderson, D.L., 1985. Lateral heterogeneity and azimuthal anisotropy of the upper mantle: Love and Rayleigh waves 100–250 s, *J. geophys. Res.,* **90,** 1842–1858.

Tarantola, A. & Valette, B., 1982. Generalized nonlinear inverse problems solved using the least squares criterion, *Rev. Geophys. Space Phys.,* **20,** 219–232.

Trampert, J. & van Heijst, H.J., 2002. Global azimuthal anisotropy in the transition zone, *Science,* **296,** 1297–1299.

Trampert, J. & Woodhouse, J.H., 2003. Global anisotropic phase velocity maps for fundamental mode surface waves between 40 and 150 s, *Geophys. J. Int.,* **154,** 154–165.

Tsuchiya, T., Tsuchiya, J., Umemoto, K. & Wentzcovitch, R.M., 2004. Elasticity of post-perovskite MgSiO$_3$, *Geophys. Res. Lett.,* **31,** L14603, doi:10.1029/2004GL020278.

Vinnik, L.P., Farra, V. & Romanowicz, B.A., 1989. Observational evidence for diffracted SV in the shadow of the Earth's core, *Geophys. Res. Lett.,* **16,** 519–522.

Vinnik, L.P., Makeyeva, L.I., Milev, A. & Usenko, Y., 1992. Global patterns of azimuthal anisotropy and deformations in the continental mantle, *Geophys. J. Int.,* **111,** 433–447.

Wang, Z. & Dahlen, F.A., 1995. Spherical spline parameterization of three-dimensional Earth models, *Geophys. Res. Lett.,* **22,** 3099–3102.

Wessel, P. & Smith, W.H.F., 1998. New, improved version of Generic Mapping Tools released, *EOS Trans. Amer. Geophys. Union,* **79,** 579.

Woodhouse, J.H., The coupling and attenuation of nearly resonant multiplets in the earth's free oscillation spectrum, *Geophys. J. R. astr. Soc.,* **61,** 261–283.

Woodward, R.L., Forte, A.M., Su, W.J. & Dziewonski, A.M., 1993. Constraints on the large-scale structure of the Earth's mantle, in *Evolution of the Earth and Planets*, pp. 89–109, eds. Takahashi, E., Jeanloz, R. & Rubie, D., Amer. Geophys. Union, Washington, DC.

APPENDIX A: ANISOTROPIC SENSITIVITY KERNELS

We parametrize our model in terms of radial anisotropy, which can be described with 5 elastic parameters, most commonly expressed as the Love parameters: A, C, L, N and F (Love 1927). We wish to extend the isotropic kernels from Woodhouse (1980) to an anisotropic medium (Mochizuki 1986; Romanowicz & Snieder 1988).

Kernels for a radially anisotropic model parametrized with the Love parameters are defined in Appendix C of Li & Romanowicz (1996). We wish to reparametrize in terms of Voigt average V_P and V_S, and the three anisotropic parameters ξ, ϕ and η. We use this parametrization due to practical concerns of the inversion process. In general, given sufficient coverage, an iterative least-squares inversion, such as the approach we use in our modelling (Tarantola & Valette 1982) has better resolution of the 3-D pattern of structure than the amplitude of that structure, due to the *a priori* damping scheme applied. If we choose a parametrization such as the Love coefficients, the anisotropy, which is the quantity we are interested in, is defined by the differences between inverted parameters. Interpreting the difference of two terms with uncertainties in amplitude from the damping procedure is very problematic both in terms of

amplitude and even sign, so we choose to invert directly for the anisotropic parameters.

To define the Voigt average equivalent isotropic velocities, we start from the definition of the equivalent Voigt average bulk and shear moduli in a radially anisotropic medium (Babuska & Cara 1991),

$$\kappa = \frac{1}{9}(C + 4A - 4N + 4F) \tag{A1}$$

$$\mu = \frac{1}{15}(C + A + 6L + 5N - 2F). \tag{A2}$$

The isotropic velocities are defined in terms of the bulk and shear moduli,

$$V_P^2 = \frac{\kappa + \frac{4}{3}\mu}{\rho} \tag{A3}$$

$$V_S^2 = \frac{\mu}{\rho}, \tag{A4}$$

and so we can substitute (A1) and (A2) into (A3) and (A4) to obtain

$$\rho V_P{}^2 = \frac{1}{15}(3C + (8 + 4\eta)A + 8(1 - \eta)L) \tag{A5}$$

$$\rho V_S{}^2 = \frac{1}{15}(C + (1 - 2\eta)A + (6 + 4\eta)L + 5N), \tag{A6}$$

where

$$\eta = \frac{F}{A - 2L}, \tag{A7}$$

which is equal to 1 in an isotropic model, and effectively describes anisotropy in the Lamé parameter λ. The relationships between the Love coefficients and observable seismic velocities are defined in eqs (1)–(4).

Note that the average isotropic velocities defined in (A5) and (A6) depend on all four of the observable seismic velocities in eqs (1)–(4), as well as η. However, in the case of small anisotropy which we assume for our perturbation-based approach, we can assume $\eta \simeq 1$, and make the first order approximation to neglect the quantity $C - A$ in comparison with $10L + 5N$ in (A6), and simplify the Voigt average velocities to

$$V_S^2 = \frac{2L + N}{3\rho} = \frac{2V_{SV}^2 + V_{SH}^2}{3} \tag{A8}$$

$$V_P^2 = \frac{C + 4A}{5\rho} = \frac{V_{PV}^2 + 4V_{PH}^2}{5}, \tag{A9}$$

such that the average isotropic S velocity depends only on V_{SV} and V_{SH}, and the P velocity only depends on V_{PV} and V_{PH}.

Taking the isotropic velocities and the anisotropic parameters ξ, ϕ, and η defined in eqs (8)–(10), we obtain the differentials,

$$\delta \ln V_S = \frac{2\delta L + \delta N}{4L + 2N} - \frac{1}{2}\delta \ln \rho \tag{A10}$$

$$\delta \ln V_P = \frac{\delta C + 4\delta A}{2C + 8A} - \frac{1}{2}\delta \ln \rho \tag{A11}$$

$$\delta \ln \xi = \delta \ln N - \delta \ln L \tag{A12}$$

$$\delta \ln \phi = \delta \ln C - \delta \ln A \tag{A13}$$

$$\delta \ln \eta = \delta \ln F - \frac{\delta A - 2\delta L}{A - 2L}. \tag{A14}$$

The sensitivity kernels for the desired parametrization will be linear combinations of the kernels described in Li & Romanowicz (1996). For convenience, we will drop the subscripts pertaining to the spherical harmonic expansion coefficients, and describe the kernel conversion in more general terms. Since we are no longer assuming a spherical harmonic expansion, we will refer to the general kernel for a relative shift in a model parameter (i.e. K_A would be the kernel describing the frequency shift due to a relative perturbation, $\delta \ln A$). Because an equivalent model perturbation should produce the same shift in mode frequency for any parametrization, we substitute eqs (A10)–(A14) into

$$K_A \delta \ln A + K_C \delta \ln C + K_L \delta \ln L + K_N \delta \ln N + K_F \delta \ln F$$
$$+ K_\rho^{(1)} \delta \ln \rho = K_{V_S} \delta \ln V_S + K_{V_P} \delta \ln V_P + K_\xi \delta \ln \xi + K_\phi \delta \ln \phi$$
$$+ K_\eta \delta \ln \eta + K_\rho^{(2)} \delta \ln \rho \tag{A15}$$

where $K_\rho^{(1)}$ refers to the density kernel for the parametrization as in Li & Romanowicz (1996), and $K_\rho^{(2)}$ is the kernel for the new parametrization, which will be different due to the inclusion of density sensitivity inside the velocity terms. Solving for the new kernels, we get

$$K_{V_S} = 2 \left(K_L + K_N - \frac{2L}{A - 2L} K_F \right) \tag{A16}$$

$$K_{V_P} = 2 \left(K_A + K_C + \frac{A}{A - 2L} K_F \right) \tag{A17}$$

$$K_\xi = \frac{1}{2L + N} \left(2LK_N - NK_L + \frac{2LN}{A - 2L} K_F \right) \tag{A18}$$

$$K_\phi = \frac{1}{C + 4A} \left(4AK_C - CK_A - \frac{AC}{A - 2L} K_F \right) \tag{A19}$$

$$K_\eta = K_F \tag{A20}$$

$$K_\rho^{(2)} = K_\rho^{(1)} + K_A + K_C + K_L + K_N + K_F. \tag{A21}$$

APPENDIX B: AUTOMATIC WAVEPACKET PICKING ALGORITHM

The early models developed using *NACT* (Li & Romanowicz 1995), were constructed using only transverse (T) component data (Li & Romanowicz 1996; Mégnin & Romanowicz 2000), the component of horizontal motion perpendicular to the great-circle path between source and receiver. Because of the relative simplicity of these waveforms, the wavepackets used in these inversions were picked by hand. Because there is no coupling with P energy, the body wave phases are, in general, well isolated, allowing for quick visual assessment of data quality and definition of wavepacket windows utilizing an interactive approach.

To develop anisotropic models we need wavepackets from all three components. The longitudinal (L) component (horizontal motion parallel with the great-circle path) and vertical (Z) component of motion measure motion of the coupled P-SV system. There are many more body wave phases on these records, as we have P phases, as well as P to S conversions such as phases that travel through the

fluid outer core, and conversions at the free surface and mantle discontinuities, which are not present on the T component. Picking isolated wavepackets is very difficult, and the definition of wavepacket windows to maximize sensitivity can be a very time-consuming task if done by hand.

In order to gather a sufficient data set of L and Z component body waveform data, we developed an automatic wavepacket picking algorithm to speed acquisition, although we review each wavepacket visually to insure data quality.

The data set includes events from 1995 to 1999 recorded on the IRIS and GEOSCOPE networks. We use events with M_W greater than 5.5, but do not use events with seismic moment greater than 10^{20} Nm ($M_W > 7.3$) in order to avoid complications from long source-time functions. In fact, all but 19 of the events used had $M_W < 7.0$, meaning that we expect source-time functions with durations generally less than 10 s, and always less than 20 s. Given that we use centroid origin times rather than hypocentral times, and the rupture time is always less than the shortest period in our data, we should account for most of the complexity from source-time functions. We also do not use traces within $15°$ of the source or the antipode, as the asymptotic calculations break down in these regions. All traces matching these criteria are then filtered to the frequency band used in the inversions. For the body waves, the short period cut-off is 32 s at present, while the long period cutoff is a function of the earthquake magnitude and ranges from 220 s to 1 h.

Each trace is then processed to select the wavepackets to be used in the inversion. First synthetics are calculated using the PREM model (Dziewonski & Anderson 1981). We define the two quantities

$$RMSR = \frac{\sum_{i=1}^{N}(d_i - s_i) \cdot (d_i - s_i)}{\sum_{i=1}^{N} d_i^2} \tag{B1}$$

$$RMSS = \frac{\sum_{i=1}^{N}(d_i - s_i) \cdot (d_i - s_i)}{\sum_{i=1}^{N} s_i^2}, \tag{B2}$$

where N is the number of data points, d_i is the ith data point, and s_i is the ith point in the synthetic trace. Data which has either of these values too large is rejected, as it is either noisy, has an incorrect instrument response, contains glitches, or is strongly affected by focusing or defocusing which we do not model in our theoretical approach.

Traces are then divided into wavepackets based on the predicted traveltimes of several phases. Wavepackets are mostly defined in the window starting just before the predicted first arrival (P, P_{diff}, or PKP) and ending just before the Rayleigh wave. For events deeper than 200 km and epicentral distances between $40°$ and $90°$, we also pick wavepackets in a window beginning after the Rayleigh wave and extending to after the predicted arrival of ScS4, which contains multiple ScS phases in the reverberative interval (Revenaugh & Jordan 1987) between the 1st and 2nd orbit Rayleigh waves.

After the wavepacket windows are defined, each packet is analysed for data quality, using a number of criteria. First, we calculate the *RMSR* and *RMSS* values, and reject packets if either value is greater than 4.0. We also calculate the ratio of maximum data and synthetic amplitudes, and reject the wavepacket if this value is greater than 2.5 or less than 0.4. A correlation coefficient is also calculated, and data is rejected if it is less than 0. Finally the packet is analysed using a moving window approach which helps eliminate data with persistent low-level noise. The *RMSR* and *RMSS* values for each packet are stored, and are utilized in the *a priori* data covariance matrix (Tarantola & Valette 1982), which is used to apply a weighting scheme to account for data noise and redundancy (Li & Romanowicz 1996).

This data selection process eliminates approximately 50 per cent of the available data, and stricter criteria can be applied on the *RMSR* and *RMSS* values at the time of inversion, if desired. This scheme allows us to gather data much more quickly, while still reviewing each packet visually to verify its quality. A similar algorithm is used for the picking of surface wavepackets (Gung 2003).